

Lawrence Berkeley National Laboratory

LBL Publications

Title

Experimental investigation into coal wettability changes caused by reactions with scCO₂-H₂O

Permalink

<https://escholarship.org/uc/item/8s84m7v3>

Authors

Li, Ke
Zhu, Chuanjie
Wan, Jiamin
et al.

Publication Date

2024-08-01

DOI

10.1016/j.jgsce.2024.205366

Peer reviewed

1 **Experimental investigation into causes of coal surface wettability** 2 **variation resulting from reaction with scCO₂-H₂O**

3 Ke Li ^a, Chuanjie Zhu ^{a*}, Jiamin Wan ^b, Tetsu K. Tokunaga ^b, Na Liu ^a, Cong Ma ^a,
4 Baiquan Lin ^a

5 ^a Faculty of Safety Engineering, China University of Mining and Technology, Xuzhou,
6 Jiangsu, 221116, China; ^b Earth and Environmental Sciences Area, Lawrence Berkeley
7 National Laboratory, Berkeley, CA, 94720, USA.

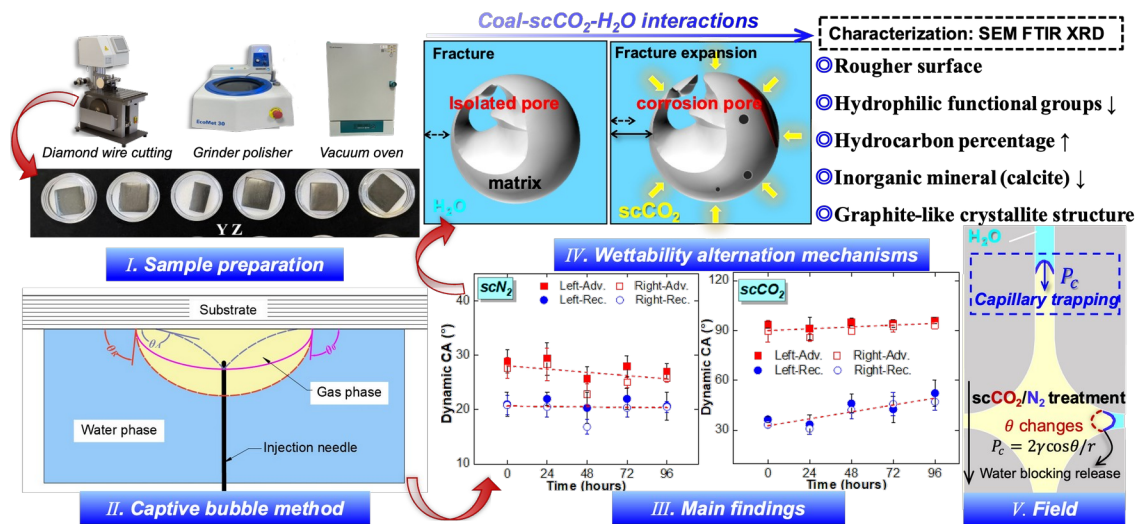
8 *Corresponding author: Chuanjie Zhu, E-mail: anq021@126.com

9 **Abstract:** Geological CO₂ sequestration (GCS) can help mitigate global warming and
10 enhance methane recovery from coal beds. However, few studies have linked the
11 effects of CO₂ to surface chemistry changes controlling wetting behavior in deep coal
12 beds. Contact angles (CAs) of CO₂/N₂-high volatile bituminous coal-H₂O systems
13 were measured under different temperatures and pressures. The surface chemistry and
14 physical structure of coals were characterized to investigate changes in
15 physicochemical properties and their relations with wettability after reactions. For N₂
16 treatment, changes in CAs were insignificant. For gaseous CO₂ treatment, the static CA
17 and the average advancing angle increased slightly. With supercritical (sc) CO₂, both
18 the static and dynamic CAs increased significantly, and θ_{adv} changed to intermediate-
19 wet (92°). Reactions with minerals exposed to scCO₂ resulted in greater surface
20 roughness and inhomogeneity, greater contact angle hysteresis and more surface sites
21 occupied by scCO₂ rather than H₂O. Increases in hydrophobic functional groups and
22 decreases in hydrophilicity were shown by FTIR spectra, reflecting the shedding of
23 polar oxygen-containing functional groups, reduction of hydrogen bonds, and
24 increasing percentage of hydrocarbons. XRD patterns obtained following scCO₂-
25 treatment showed that crystallite growth and molecular polymerization were higher
26 toward graphite-like. The calculated structural parameters of functional groups and
27 crystallites both showed elevated coal rank. Changes in crystallite structure, notably
28 higher carbon content and decreased negative surface charge, are unfavorable for
29 water-wetting. This study contributes to understanding surface chemistry changes
30 responsible for decreased wettability during CO₂-enhanced coal bed methane recovery
31 and GCS in coal reservoirs.

32 33 **Highlights**

- 34 (1) Wettability of coal treated by scCO₂ changed significantly but not by gas-N₂/CO₂
35 and scN₂.
36 (2) Under scCO₂ treatment, static contact angle changes stabilized at after 48 hours.
37 (3) ScCO₂ treatment decreased abundance of hydrophilic functional groups.
38 (4) Rougher surface caused by scCO₂ treatment generated greater contact angle

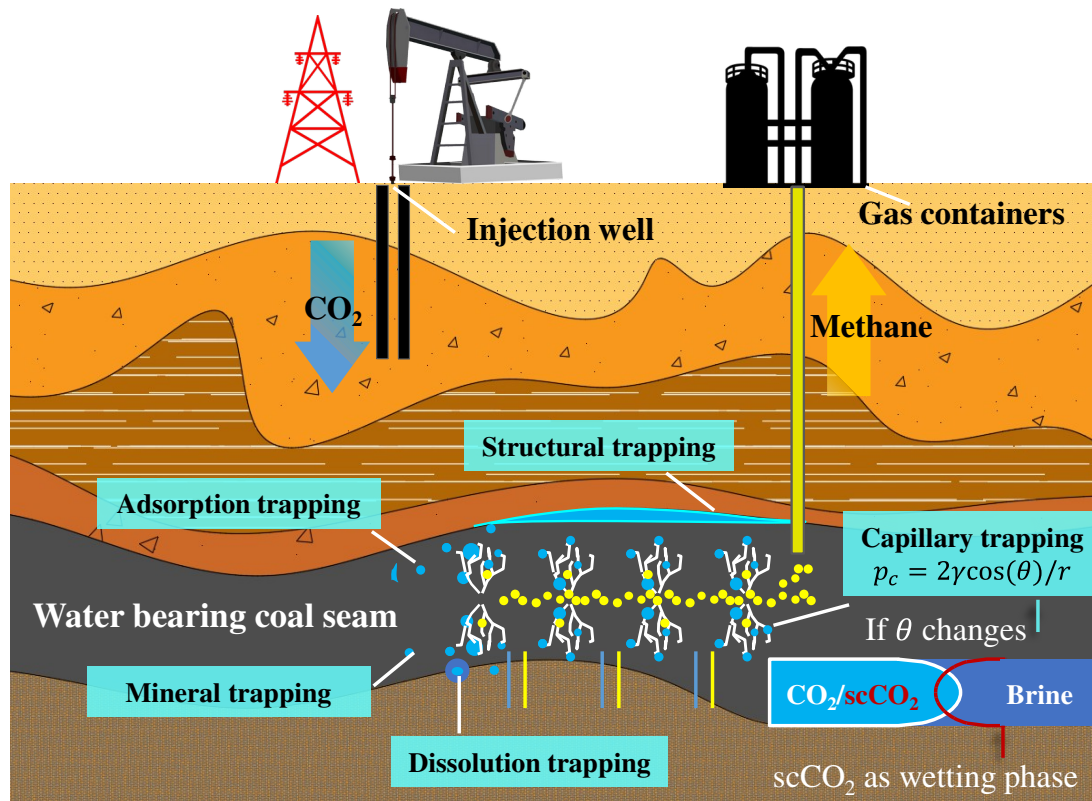
39 hysteresis.
 40 (5) ScCO₂ treatment depleted the inorganic minerals in coal (most notably calcite).
 41
 42 **Keywords:** High volatile bituminous coal; Wetting; Contact angle; Supercritical CO₂;
 43 Functional groups; Minerals; Crystallite structure
 44
 45 **Graphical abstract**



46
 47

48 1 Introduction

49 Geological CO₂ sequestration (GCS) in coal beds provides advantages of CO₂
 50 storage and enhanced coal bed methane recovery (CO₂-ECBM) (Hadi Mosleh et al.,
 51 2017). Thus CO₂ enhanced oil recovery (CO₂-EOR) and CO₂-ECBM are widely
 52 studied and commercially applied (Godoi and Matai, 2021). CO₂-ECBM has unique
 53 advantages resulting from coal matrix micropore development that favors adsorption
 54 of CO₂ relative to CH₄ (X. Liu et al., 2023). Thus, adsorption trapping is the most prominent
 55 trapping mechanism in coal reservoirs (Iglauer, 2011). Wettability is an important
 56 factor which affects the potential and efficiency of CO₂ trapping and methane recovery
 57 as shown in **Figure 1** (Tokunaga et al., 2013).



58 ● scCO₂ ● Methane ● Brine

59 **Figure 1** GCS with five main trapping mechanisms and CO₂-ECBM in deep coal
 60 reservoirs, where the efficiency of geological storage (especially capillary and
 61 structure trapping) and methane recovery displacement depend on wettability.

62

63 Minerals show different affinities for H₂O and wettability becomes complicated
 64 after CO₂ injection into water-bearing reservoirs (Fatah et al., 2021a). Previous studies
 65 reported on the wettability of CO₂-treated minerals (Jung and Wan, 2012; Sun and
 66 Bourg, 2023; Tenney and Cygan, 2014), in particular mica (muscovite), quartz or
 67 silica, feldspar, calcite, kaolinite, smectite. For coal which is composed of multiple
 68 minerals as shown in Table A. 1, wettability is also affected by coal rank and mineral
 69 component content (Arif et al., 2016b; Shojai Kaveh et al., 2012), which reflect
 70 differences in physicochemical properties of surfaces.

71 Wettability has been widely investigated as a function of reservoir conditions
 72 (temperature, pressure, salinity, ion type/strength, and fluid composition) (Shojai
 73 Kaveh et al., 2016, 2011). Arif et al. (2016a) reported that the advancing and receding
 74 angles of mica (surface roughness ~12 nm) exposed to CO₂ were positively correlated
 75 with pressure and salinity, and negatively correlated with temperature. The advancing
 76 contact angle (CA) at 20 MPa and 308 K was ~110°, and water-wet surfaces became
 77 CO₂-wet. Iglauer et al. (2012) used molecular dynamics to simulate contact angles in
 78 CO₂-H₂O/NaCl-quartz systems as a function of pressure at 300 K and 350 K, and
 79 reported that contact angles increased significantly with pressure and weakly with
 80 salinity at subcritical and supercritical states. Chen et al. (2015) investigated contact

81 angles of quartz under different ionic strengths (divalent ion Ca^{2+} and monovalent ion
82 Na^+). Ibrahim and Nasr-El-Din (2016) measured the zeta potential of high volatile
83 bitumen coal (hvBb) under different NaCl concentrations by a phase-analysis light-
84 scattering technique. Roshan et al. (2016) conducted experiments under various ion
85 types (NaCl , KCl , MgCl_2 , CaCl_2) and concentrations (0.1, 0.5, and 1 M). Zheng et al.
86 (2020) used nuclear magnetic resonance (NMR) as a non-invasive method to study
87 effects of water status (adsorbed-water, free-water) on wettability, and found that free-
88 water decreased CO_2 wetting and the sensitivity of wettability to pressure.

89 Previous work explained wettability mainly through influences of molecular density
90 (Arif et al., 2016a), pore adsorption (Sun et al., 2022), interfacial tension, surface
91 charge, and organic matter (Shojai Kaveh et al., 2012). The increase of molecular
92 density implied that the probability of collision increases between H_2O molecules and
93 C molecules (Liu et al., 2010), and H_2O molecules are more likely to be trapped on the
94 surface. Zhu et al. (2019) reported that the dependence of adsorption isotherms on
95 temperature and pressure is consistent with changes in the contact angle. Equilibrium
96 contact angle can be calculated by combining the interfacial tension (IFT) values
97 between different phases with the modified equation of state (EOS) and Young-
98 Laplace equation (Shojai Kaveh et al., 2016). However, while adsorption and
99 interfacial tension are parameters correlated with wettability, it is desirable to identify
100 underlying mechanisms. The reduction of negative surface charge decreases
101 electrostatic repulsions (electric double layer theory (Tokunaga, 2012)), which
102 consequently affects water film stability and wettability. Fatah et al.(Fatah et al.,
103 2021a) reported that scCO_2 may dissolve clay and carbonate minerals and transform
104 the clay-rich shale to become CO_2 -wet. Arain et al. (2023) reported that trace amounts
105 of hydrocarbons on coal surfaces like dissolved organic matter (Ali et al., 2022) altered
106 wettability of rocks. Crawford et al. (1994) concluded that the effect of oxygen-
107 containing functional groups on wettability cannot be ignored. Gathitu et al. (2009)
108 found that coal exposed to CO_2 may lead to new carbon structure and rearrange
109 macromolecules.

110 Previous work evaluated wettability of various minerals as a function of reservoir
111 conditions. However, studies on the mechanisms of wettability alteration of coal
112 exposed to scCO_2 - H_2O are limited, and few have linked wetting behavior with surface
113 chemistry. The surface wettability is complex due to the differences in structure and
114 components between coal and pure, natural minerals. Furthermore, the interactions
115 between coal and CO_2 - H_2O also affect the wettability. Wettability variations introduce
116 a large uncertainty into the prediction of trapping CO_2 , methane displacement
117 capacity, CO_2 storage height, and CO_2 containment security. Therefore, it is crucial to
118 determine the potential effects of chemical reactions on wettability and the changes in
119 physical structure (porosity, roughness) and surface chemistry (functional groups,
120 crystal structure) of coal surface.

121 In this work, we measured in-situ static/dynamic contact angles of high volatile B
122 bituminous (hvBb) medium rank coal under N_2/CO_2 treatment at different

123 temperatures, pressures, and exposure times to determine the extent to which changing
 124 these conditions alter wettability. We then analyzed physicochemical properties via
 125 characterization methods (FTIR, XRD, SEM) in order to identify underlying surface
 126 processes responsible for wettability alteration. This study provides measurements-
 127 based theoretical guidance for field practices, including the choice of solvents or
 128 nanofluids injected to improve CO₂ trapping, and further deepens the understanding of
 129 wetting behavior to enhance CO₂-ECBM and GCS.
 130

131 2 Experiments

132 2.1 Experimental method and materials

133 2.1.1 Coal sample and preparation

134 A high volatile B bituminous (hvBb) medium rank coal was collected from
 135 Yuanzhuang (YZ) coal mine in Huaibei, China. The proximate analysis of coal
 136 samples is shown in **Table 1**. The coal samples were prepared by block-cutting
 137 method, i.e., large coal blocks were cut into smaller square slices with dimensions of
 138 ~21mm×21mm×3-4mm (thickness), and then coal surfaces were ground and polished.
 139 Some prepared coal samples are shown in **Figure 2a**.

140 Coal surfaces were polished with a series of silicon carbide sandpapers (220-3000
 141 grit). Small scratches were first removed with 220-320 grit sandpapers, followed by
 142 careful water polishing with 400-3000 grit sandpapers to complete the sample surface
 143 preparation. We used deionized water to reduce surface charge interference. Sample
 144 surfaces were finally cleaned with AccuDuster III 2510 before experiments.
 145

146 **Table 1** Proximate analysis results of coal sample.

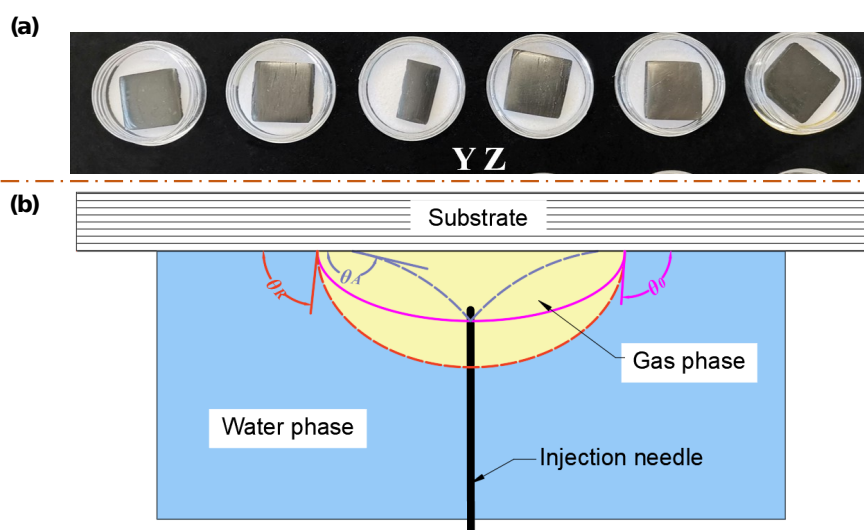
Coal sample	M _{ad} (%)	A _{ad} (%)	V _{daf} (%)	FC _{ad} (%)	Coal type
YZ	2.58	9.16	36.75	57.46	hvBb coal

147 Note: M_{ad}—the moisture content on air-dried basis, A_{ad}—the ash content on air-dried basis, V_{daf}—
 148 the volatile matter content on dry-ash-free basis, FC_{ad}—the fixed carbon content on air-dried basis.
 149

150 2.1.2 Contact angle measurement

151 Dynamic and static contact angle (CA) measurements are commonly measured by
 152 three main methods: sessile drop (Drelich, 2013), pendant drop (Bhutani et al., 2012),
 153 and captive bubble (Chau, 2009). We used the captive bubble method to measure CAs
 154 (**Figure 2b**), where bubbles were captured beneath a solid substrate submersed in the
 155 aqueous phase under precise control of P/T (Wan et al., 2014). Due to surface
 156 heterogeneity of substrates, we measured advancing/receding angles (θ_A & θ_R) on both
 157 the left and right sides as shown in **Figure 2b**. The CAs reported in this study were all
 158 water contact angles, which are measured between the solid-water and nonaqueous
 159 fluid-water interfaces. After a bubble captured by the coal substrate separated from the
 160 injection needle, we began to photographically record images, which were later

161 processed with Image J to measure static CAs.



162

163 **Figure 2** Experimental samples and contact angle measurement. (a) Polished YZ coal
164 samples, (b) Schematic of contact angle measurement by the captive bubble method.
165 Young's equilibrium contact angle θ_0 , advancing contact angle θ_A , receding contact
166 angle θ_R . Usually, $\theta_A > \theta_0 > \theta_R$, thus θ_0 is constrained by θ_A and θ_R .

167

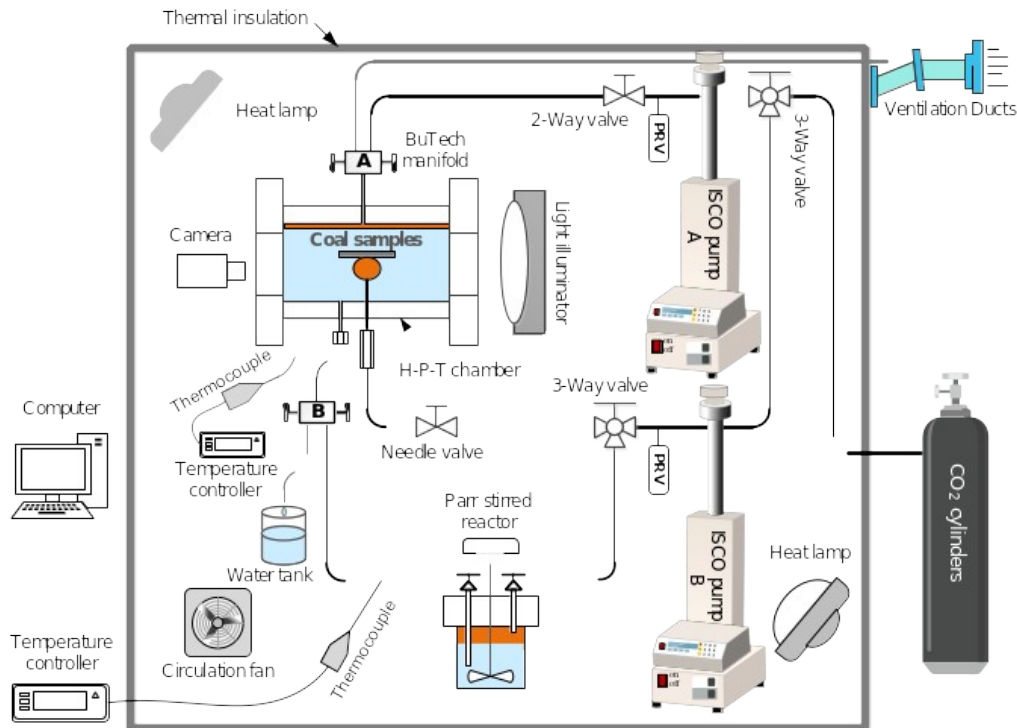
168 2.2 Experiment setup and procedure

169 2.2.1 Experiment setup

170 The experimental system shown in **Figure 3** includes: a high pressure and
171 temperature (P-T) chamber, stirred reactor, pressure control unit (pump, gas cylinder),
172 temperature control unit (temperature controller, thermocouple, heat lamp, circulation
173 fan, and thermal insulation), and experimental information acquisition unit (camera,
174 computer, and light illuminator).

175 The high P-T viewing chamber (IFT-10, Core Laboratories) can support a maximum
176 working pressure and temperature of 690 bar and 450 K, respectively. An inlet in the
177 upper portion of the chamber is connected to a two-stem manifold (A), one of which is
178 connected to an exhaust pipe to safely vent CO_2 into the ventilation ducts, and the
179 other is connected to a pump (A) that provides back pressure. The bottom of the
180 viewing chamber has two inlets, one of which is connected to a needle valve to
181 generate CO_2 bubbles. The needle valve is connected to pump (B) via a three-way
182 valve for controlling the flow rate of CO_2 . The other inlet is connected to a two-stem
183 manifold (B) which connects a stirred reactor and a water tank.

184 Coal samples are placed on a stainless-steel plate near the upper center of the
185 viewing chamber. Two glass windows that are resistant to high temperature and
186 pressure are installed on opposite sides of the chamber to enable transmission of the
187 illuminator's light into the chamber for recording images of the droplets. The entire
188 experimental system is enclosed in a thermally insulated box to maintain a constant
189 temperature regulated by a temperature controller.



190



191

192 **Figure 3** Schematic diagram of the experimental system and photograph of the
 193 experimental setup for contact angle measurements.

194

195 2.2.2 Contact angle measurement procedures

196 (a) Preparation before CO₂ releasing. We clamped a coal substrate onto the lower
 197 surface of a stainless-steel plate, and then immersed it in high pressure deionized
 198 water (20 bar) for a minimum of 48 hours to fill its pores with water. The thermally
 199 insulated box and viewing chamber were then heated to the desired temperature. The
 200 viewing chamber was pressurized to the desired pressure using pump (A) with CO₂.

201 The reactor was equilibrated to fully dissolve CO₂ in water, then further stirred for
 202 30 minutes in preparation for transfer of CO₂-saturated water into the viewing
 203 chamber. The two pumps were set to a constant pressure difference between injection
 204 pressure and back pressure. We then opened the valve between the stirred reactor and

205 the viewing chamber to allow CO₂-saturated deionized water to flow into the chamber
206 and displace the original water. Solubility equilibrium was again established for more
207 than 1 hour.

208 (b) CO₂ captured by coal substrate. CO₂ bubbles were released from the stirred
209 reactor through the needle valve and captured upon buoyant contact against the
210 overlying coal substrate. In order to measure dynamic contact angles, the CO₂ bubbles
211 advanced through the pressure difference between the reactor and the viewing
212 chamber, and receded through lowering the pressure of the pump (B). The rate of
213 expansion and contraction of the bubbles was controlled with the needle valve.

214 After each measurement, the pressure chamber was tilted to remove the captured
215 CO₂ bubbles from the substrate. After a period of reaction, new CO₂ bubbles were
216 then released at the same position after dissolution equilibrium. More detailed
217 experiment procedures can be found in our previous work (Zhu et al., 2019).

218 2.3 Characterization methods of physicochemical property

219 (1) Surface functional group

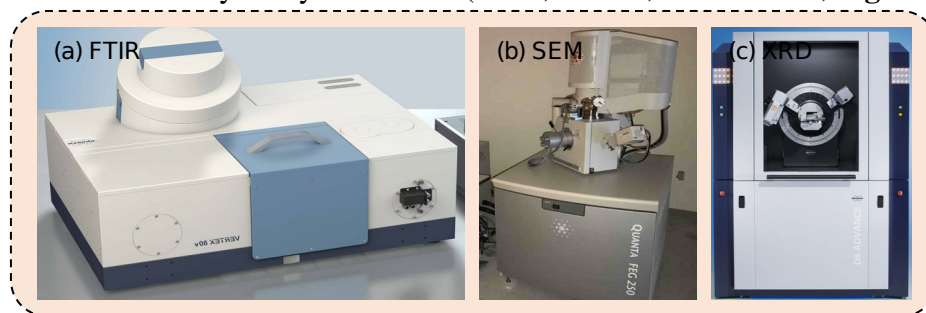
220 The surface functional group chemistry of coal surfaces was measured by Fourier
221 Transform Infrared spectroscopy (FTIR) using VERTEX 80v (Germany, Bruker) as
222 shown in **Figure 4a**. The measurement was conducted by attenuated total reflection
223 (ATR).

224 (2) Coal surface micromorphology

225 Surface micromorphological of the coal samples was characterized by scanning
226 electron microscopy (FEI Quanta TM 250, **Figure 4b** with a magnification of 6–100
227 million and an accelerating voltage of 0.2–30 kV).

228 (3) Crystallite structure

229 Coal is a long-range disordered and short-range ordered amorphous crystal.
230 Information on the size, shape, and structure of the ordered crystallite structure can be
231 calculated by diffraction intensity and diffraction angle. The samples were dried to
232 remove water in a vacuum oven before characterization. Crystallite structures of coal
233 were then determined by X-ray diffraction (XRD, Bruker, D8 Advance, **Figure 4c**).



234

235 **Figure 4** Experimental setup for the characterization of physicochemical properties.
236 (a) VERTEX 80v FTIR; (b) FEI Quanta TM 250 SEM; (c) D8 Advance XRD.

237

238 2.4 Experiment design

239 Factors affecting wettability of coal include physical and chemical properties of coal

240 (mainly surface functional groups and mineral components) and environmental
 241 conditions (temperature and pressure). In the process of CO₂ injection into water-
 242 bearing coal seams for storage or methane displacement, high pressure or chemical
 243 reaction may impact the physical and chemical structure of coal surfaces, and thereby
 244 affect the wettability of coal.

245 In this study, wettability changes over time were measured following coal exposure
 246 to low pressure (gaseous) and high pressure (supercritical) CO₂. Due to the poor water
 247 solubility of CO₂ under low pressure conditions, its impact on the physical and
 248 chemical properties of the coal surface may be not significant, but under high pressure
 249 conditions, CO₂ dissolved in water will form an acidic solution, which may have a
 250 greater impact on the physical and chemical properties of coal surface. N₂ (the most
 251 chemically stable of the known diatomic molecules) is much less soluble in water, so
 252 the chemical reaction between its aqueous solution and coal is negligible. Therefore,
 253 we also measured the wettability variation of coal surfaces exposed to N₂ under the
 254 same experimental conditions, in order to determine the influence of coal reaction
 255 with CO₂ aqueous solutions on wettability. The specific experimental conditions are
 256 shown in **Table 2**.

257

258 **Table 2** Experimental conditions.

Type	Critical point	Gas phase	Supercritical phase
N ₂	$P=34.0$ bar, $T=-147.0^{\circ}\text{C}$	$\sim 23^{\circ}\text{C}$, 20 bar	45°C , 120 bar
CO ₂	$P=73.8$ bar, $T=31.2^{\circ}\text{C}$	$\sim 23^{\circ}\text{C}$, 20 bar	45°C , 120 bar

259

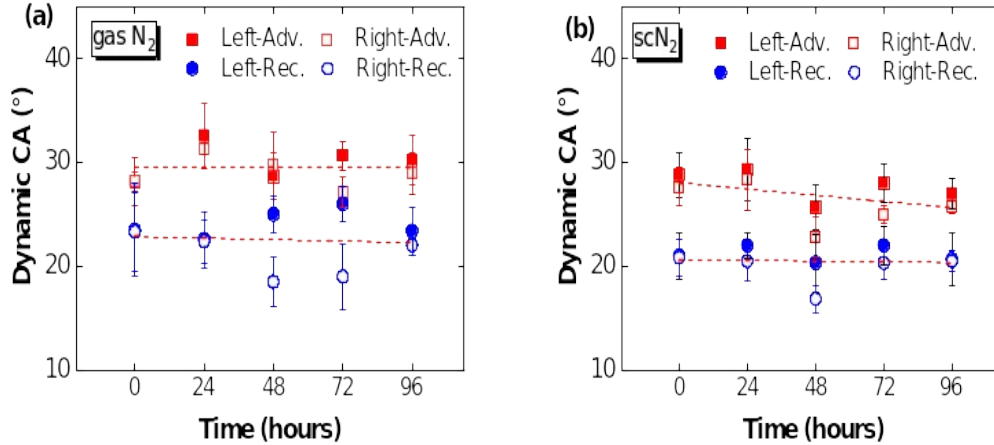
260 **3 Results**

261 **3.1 Coal-N₂-H₂O competitive wetting**

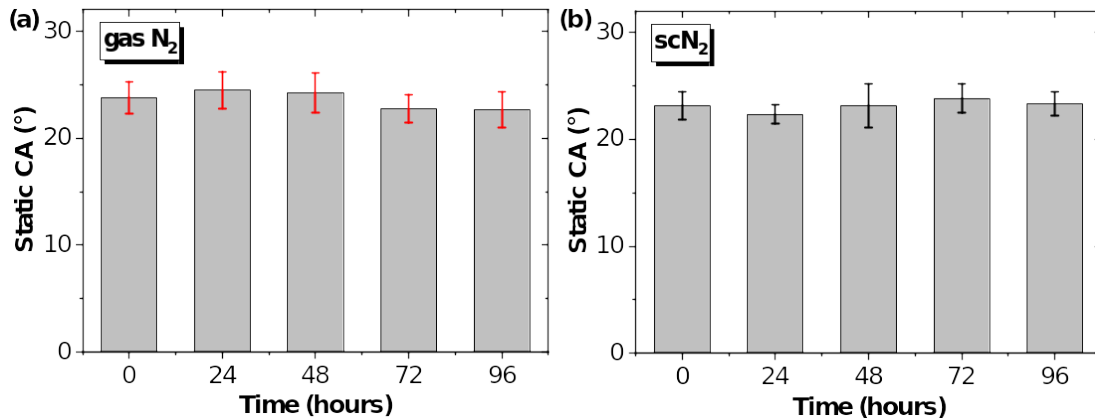
262 **Figure 5** gives time-dependent dynamic contact angles for N₂-H₂O-coal systems
 263 (values are given in **Table A.3** and **Table A.4**). For gaseous N₂ ($P=20$ bar, $T=25^{\circ}\text{C}$),
 264 the average advanced (θ_{adv}) and receding (θ_{rec}) contact angles are $28\sim 32^{\circ}$ and $22\sim 23.5^{\circ}$,
 265 respectively, indicating strong water-wetting. The variation of contact angles was less
 266 than 5° , indicating that time-dependent wettability of coal in gaseous N₂-H₂O-coal
 267 systems is stable under low pressure. For scN₂ ($P=120$ bar, $T=45^{\circ}\text{C}$), the θ_{adv}
 268 ($24.5\sim 28.5^{\circ}$) and θ_{rec} ($18.5\sim 21.5^{\circ}$), also changed very slightly and were close to values
 269 under low pressure due to slight variation of density (Zhu et al., 2019). The static
 270 contact angles for gaseous N₂ and scN₂ are $23\sim 25^{\circ}$ and $22\sim 24^{\circ}$, respectively, which
 271 follow similar trends as dynamic contact angles, as shown in **Figure 6**.

272 Gas or supercritical N₂ is relatively insoluble in water and cannot form acid solution
 273 that react with coal under the current experimental condition. The calculated solubility
 274 of N₂ in water is $\sim 9.76\times 10^{-5}$ mol/mol at 120 bar and 45°C (Battino et al., 1984).
 275 Therefore, the only factor that may affect wettability is the high pressure. The applied
 276 high pressure is expected to change pore structure of coal (such as pore compaction,

277 pore expansion) or generate fractures (Jia et al., 2022; Wang et al., 2022). However,
 278 based on the results of time-dependent dynamic and static contact angles, these
 279 physical changes of coal surface caused by high pressure N₂ did not have a significant
 280 effect on wettability.



281
 282 **Figure 5** Time-dependent dynamic CAs with N₂ treatment. (a) Dynamic contact angle
 283 under gaseous N₂ ($P=20$ bar, $T=25^{\circ}\text{C}$), (b) Dynamic contact angle under scN₂ ($P=120$
 284 bar, $T=45^{\circ}\text{C}$). “Left-Adv” and “Right-Adv” refer to the advancing contact angles
 285 measured on the left and the right side of bubbles, respectively.



286
 287 **Figure 6** Time-dependent static CAs. (a) Static contact angle under gaseous N₂ ($P=20$
 288 bar, $T=25^{\circ}\text{C}$), (b) Static contact angle under scN₂ ($P=120$ bar, $T=45^{\circ}\text{C}$).

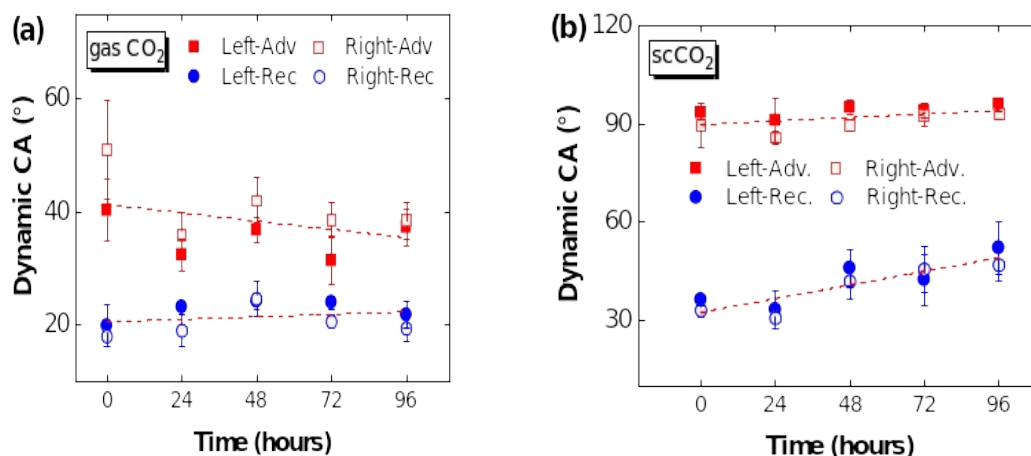
289

290 3.2 Coal-CO₂-H₂O competitive wetting

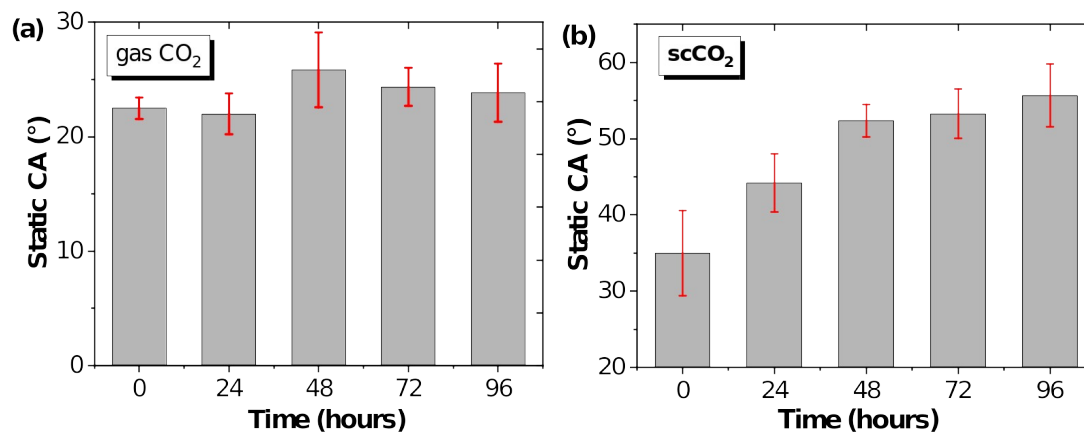
291 The time-dependence of dynamic contact angles (CAs) exposed to gas and
 292 supercritical CO₂-H₂O systems are presented in **Figure 7**. For gaseous CO₂, the
 293 average advancing contact angles (θ_{adv}) varied from 34.1° to 45.7°. The dynamic CA at
 294 0 hour was the highest (with an average value of 45.7°), followed by θ_{adv} decreasing
 295 with time. However, dynamic advancing CAs for gaseous CO₂ varied little (~5.3°)
 296 from 24 hours to 96 hours, and average receding contact angles (θ_{rec}) changed slightly
 297 (19° to 24°). In contrast, for scCO₂, both θ_{adv} and θ_{rec} show obvious increases over
 298 time, especially for the θ_{rec} which increased from 35° (0 hour) to 50° (96 hours). The

299 θ_{adv} with scCO₂ changed from water-wet to intermediate-wet.

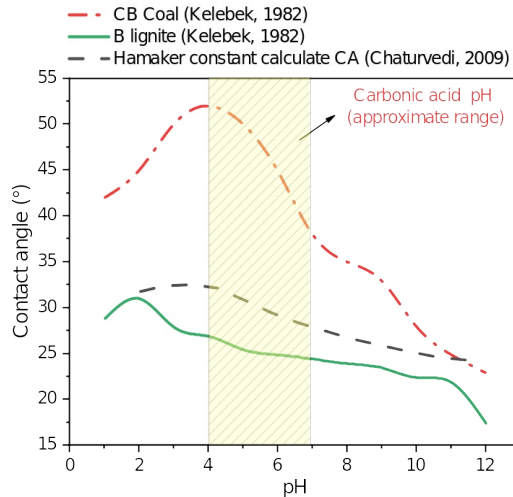
300 We also measured the time-dependence of static contact angles (CA) as shown in
301 **Figure 8**. Average static CAs in gaseous CO₂ fluctuated between 22° and 26°, while
302 those in scCO₂ increased dramatically from 35° (0 hour) to 56° (96 hours).
303 Additionally, the static CA in scCO₂ tends to be stable after 48 hours of reaction. The
304 greater CA after scCO₂ treatment is attributed to decrease in pH and more extensive
305 mineral reactions, as will be discussed in section 4.1. The increases in CA with
306 decreasing pH in carbonate solution is consistent with a previous report (Chaturvedi et
307 al., 2009) (4<pH<7) as shown in **Figure 9**.
308



309 **Figure 7** Time-dependent dynamic contact angles with CO₂ treatment. (a) Dynamic
310 CA under gaseous CO₂ ($P=20$ bar, $T=25^{\circ}\text{C}$), (b) Dynamic CA under scCO₂ ($P=120$
311 bar, $T=45^{\circ}\text{C}$).
312



313 **Figure 8** Time-dependent static contact angles. (a) Static CA under gaseous CO₂
314 ($P=20$ bar, $T=25^{\circ}\text{C}$), (b) Static CA under scCO₂ ($P=120$ bar, $T=45^{\circ}\text{C}$).
315



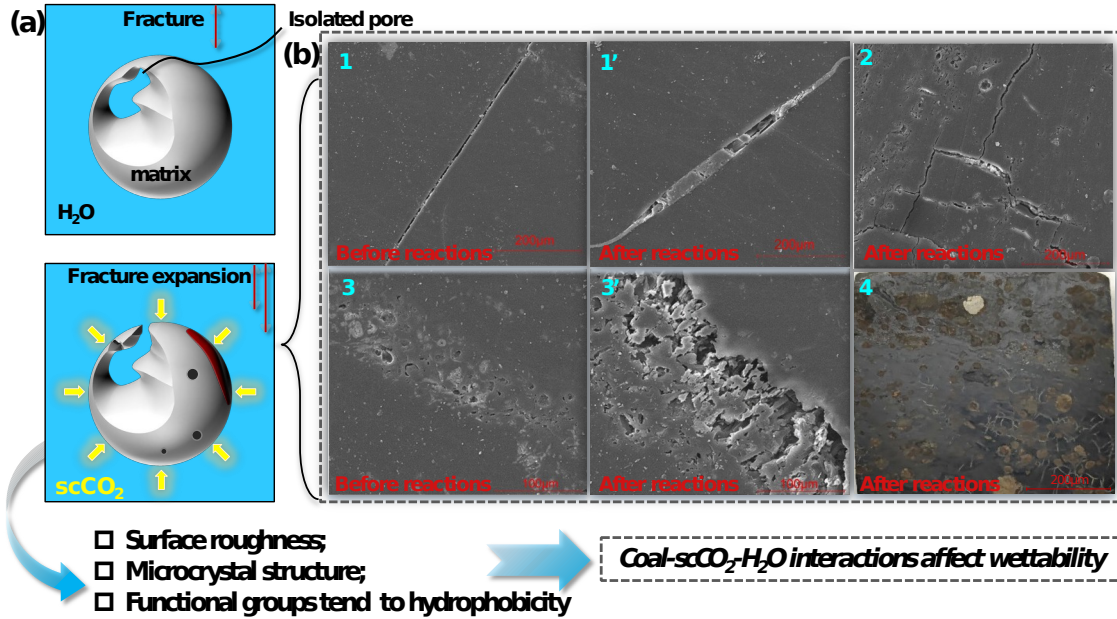
316

317 **Figure 9** Experimental and calculated contact angles of CB coal and B lignite coal
 318 samples with pH (Kelebek, 1982), and calculated CA (Chaturvedi et al., 2009). pH
 319 depends on solute concentration and ionization equilibrium constant in the solution,
 320 and the pH of carbonic acid usually ranges from 4–7 (MacInnes and Belcher, 1933).
 321

322 4 Discussion

323 4.1 Coal surface micromorphology

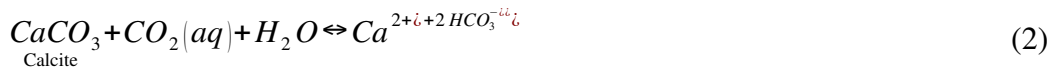
324 The coal-scCO₂-H₂O interaction affects wettability through three main
 325 physicochemical mechanisms shown in **Figure 10a**. Surface roughness has a potential
 326 effect on specific surface area and surface free energy, which consequently affects
 327 wettability (Wei et al., 2022). After scCO₂ treatment, the appearance of corrosion
 328 pores, connecting partially isolated pores, fracture extension, and edge warping in
 329 **Figure 10b** changed surface roughness and pore structure, which resulted from
 330 chemical reactions between minerals and the weakly acidic solution. CO₂ dissolved in
 331 water produces H⁺ and HCO₃⁻ ions in acidic systems (Lerman and Mackenzie,
 332 2018) as shown in Eq.(1). These ions, along with H₂O and CO₂ molecules, altered the
 333 mineral composition (mineral composition of raw coal as shown in **Table A. 1**)
 334 through reaction Eqs.(2)–(5) (Ao et al., 2017; Labus and Bujok, 2011). The
 335 dissolution of the minerals, especially hydrophilic clay and carbonate minerals, has
 336 been also reported in previous studies (Fatah et al., 2021b; Lu et al., 2021). The
 337 brownish-yellow substance in **Figure 10b** is FeO(OH), which was produced by Fe
 338 oxidation of ferrous carbonate to FeO(OH) in the carbonic acid solution.
 339



340

341 **Figure 10** The changes of physicochemical property exposed to scCO₂. (a) Schematic
 342 diagram of three mechanisms for the effect of coal-scCO₂-H₂O interactions on
 343 wettability. (b) Coal surface micrographs: (1–1') fracture extension before and after
 344 reactions with scCO₂; (2) edge warping after reactions with scCO₂; (3–3') corrosion
 345 pores and connection of isolated pores before and after reactions with scCO₂; (4)
 346 brownish-yellow FeO(OH) after reactions with scCO₂. Note: Some of the
 347 micrographs in Figure 10 (b) served as the basis for drawing the mechanism
 348 schematic in our recently published paper (S. Liu et al., 2023).

349

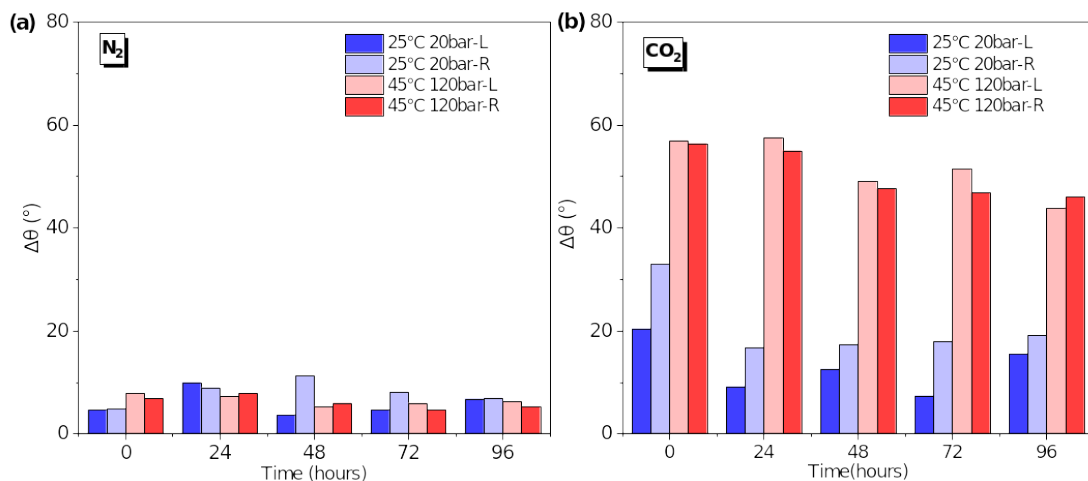


350

351 Additionally, adsorption sites of coal surface increased after reaction with scCO₂
 352 since surface fractures are developed and connected (Chen et al., 2019). The higher
 353 concentration of CO₂ molecules convert some H₂O-occupied sites to CO₂-occupied
 354 sites (Yu et al., 2022), partially displacing the adsorbed water and transforming the
 355 coal surface into a heterogeneous surface comprising of solid and CO₂-occupied
 356 pockets (Sun et al., 2022). The adsorption and interaction energy of CO₂ molecules
 357 are enhanced in the supercritical state on the coal surface (Liu et al., 2010), which
 358 causes CO₂ to accumulate as a thin film at the solid/liquid interface (Iglauer et al.,
 2012; Xu et al., 2023). The chemical reactions of minerals resulted in a rougher coal

359 surface which promotes CO₂ adsorption, and this interfacial behavior favors CO₂-
 360 wetting (Zhou et al., 2022).

361 Contact angle hysteresis, or the difference between θ_{adv} and θ_{rec} denoted by $\Delta\theta$,
 362 results from variation of surface roughness, chemical inhomogeneity, and pinning
 363 effects (Cai and Song, 2021; Kulinich and Farzaneh, 2009). The average $\Delta\theta$ s of coal
 364 for gaseous N₂ and scN₂ treatment were 7.0° and 6.3° as in **Figure 11a**, respectively,
 365 which were obviously smaller than those of coal for CO₂ treatment as shown in **Figure**
 366 **11b**. The average $\Delta\theta$ of coal was 16.8° for gaseous CO₂ treatment, while it increased
 367 to 52.6° for scCO₂ treatment. The mole fraction of CO₂ solubility in water ranges from
 368 0.695×10^{-3} in the gaseous state (T=20°C, P=1 bar) to 2.51×10^{-3} in the supercritical
 369 state (T=50°C, P=85.1 bar) (Sabirzyanov et al., 2002). Differences in $\Delta\theta$ indicate that
 370 chemical reactions resulted in greater surface inhomogeneity of coal after reaction
 371 with scCO₂.



372

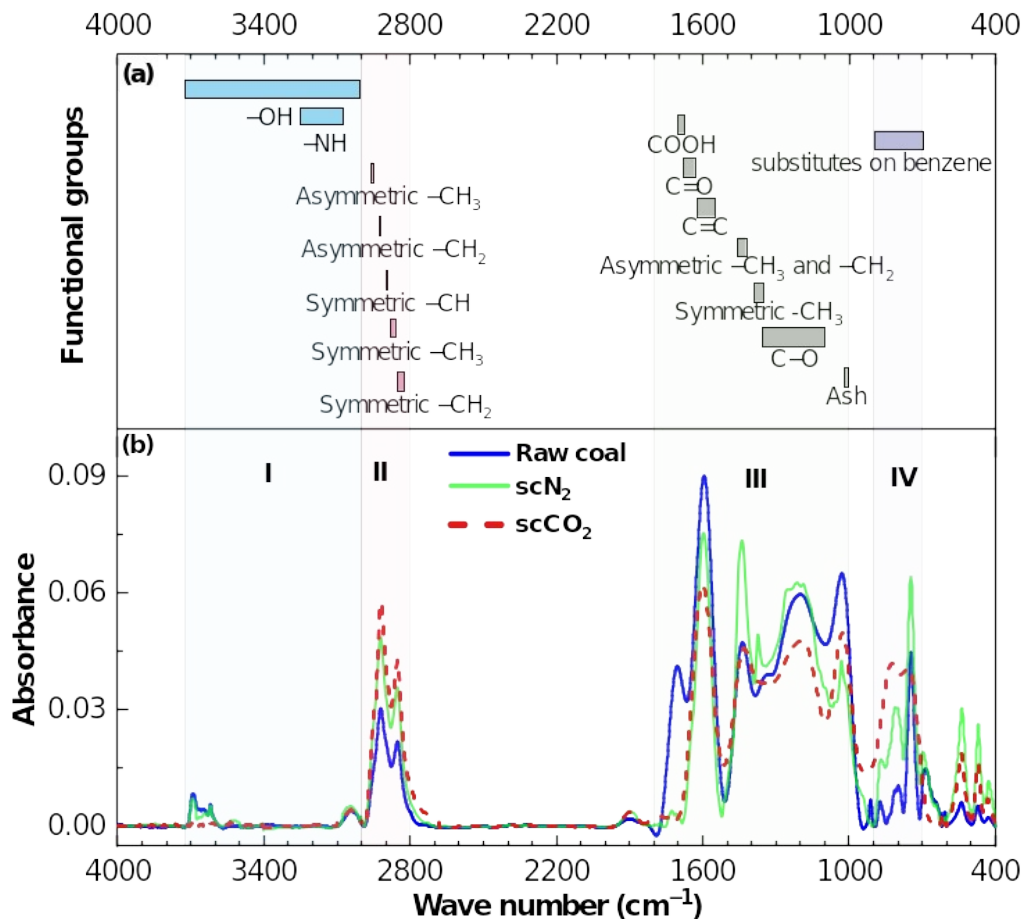
373 **Figure 11** Contact angle hysteresis denoted by $\Delta\theta$ with time for CO₂ and N₂
 374 treatment under different pressures and temperatures, respectively. “L” and “R” refer
 375 to CA measurements on the left and the right side of bubbles, respectively.

376

377 4.2 FTIR functional groups

378 Surface roughness mainly reflects physical structure, and the influence of surface
 379 chemistry (functional groups, crystallite structure) on wettability also needs to be
 380 further discussed. The FTIR spectra of coal are usually divided into four absorption
 381 bands (Lu et al., 2021), i.e., hydroxyl groups (3700–3200 cm⁻¹), aliphatic
 382 hydrocarbons (3000–2800 cm⁻¹), oxygen-containing groups (1800–1000 cm⁻¹), and
 383 aromatic hydrocarbons (900–700 cm⁻¹). The assignment of functional groups in each
 384 absorption band is shown in **Figure 12a**. **Figure 12b** gives FTIR spectra of raw coal,
 385 and coal with H₂O treated by scN₂ or scCO₂ at T=45°C and P=90 bar after 96 hours,
 386 respectively. Absorption peaks of three group experiments had similar peak shape but
 387 different peak intensity and area, indicating that the content of functional groups
 388 changed but types of functional group and macromolecular structure remained
 389 basically similar (Shang et al., 2021). Due to the influence of algorithms, samples, and

390 setups, absorption peaks in the same band could still be shifted and overlapped (Wang
 391 et al., 2017). Previous studies disputed assignment of different peak positions to the
 392 same functional group (Yan et al., 2020), so we used integral areas of sub-peaks rather
 393 than peak intensity to determine types and content of functional groups. The fitted
 394 curves were decomposed into sub-peaks controlled by Gaussian or Lorentz algorithms
 395 with the correlation coefficient $R^2 > 0.98$.



396

397 **Figure 12** The FTIR spectra and assignment of functional groups. (a) Assignment of
 398 functional groups of coal surface in the range of 4000–400 cm^{-1} . (b) The FTIR spectra
 399 of raw coal, scN_2 , and scCO_2 were divided into four absorption bands: **I**—Hydroxyl
 400 groups, **II**—Aliphatic hydrocarbons, **III**—Oxygen-containing groups, **IV**—Aromatic
 401 hydrocarbons.

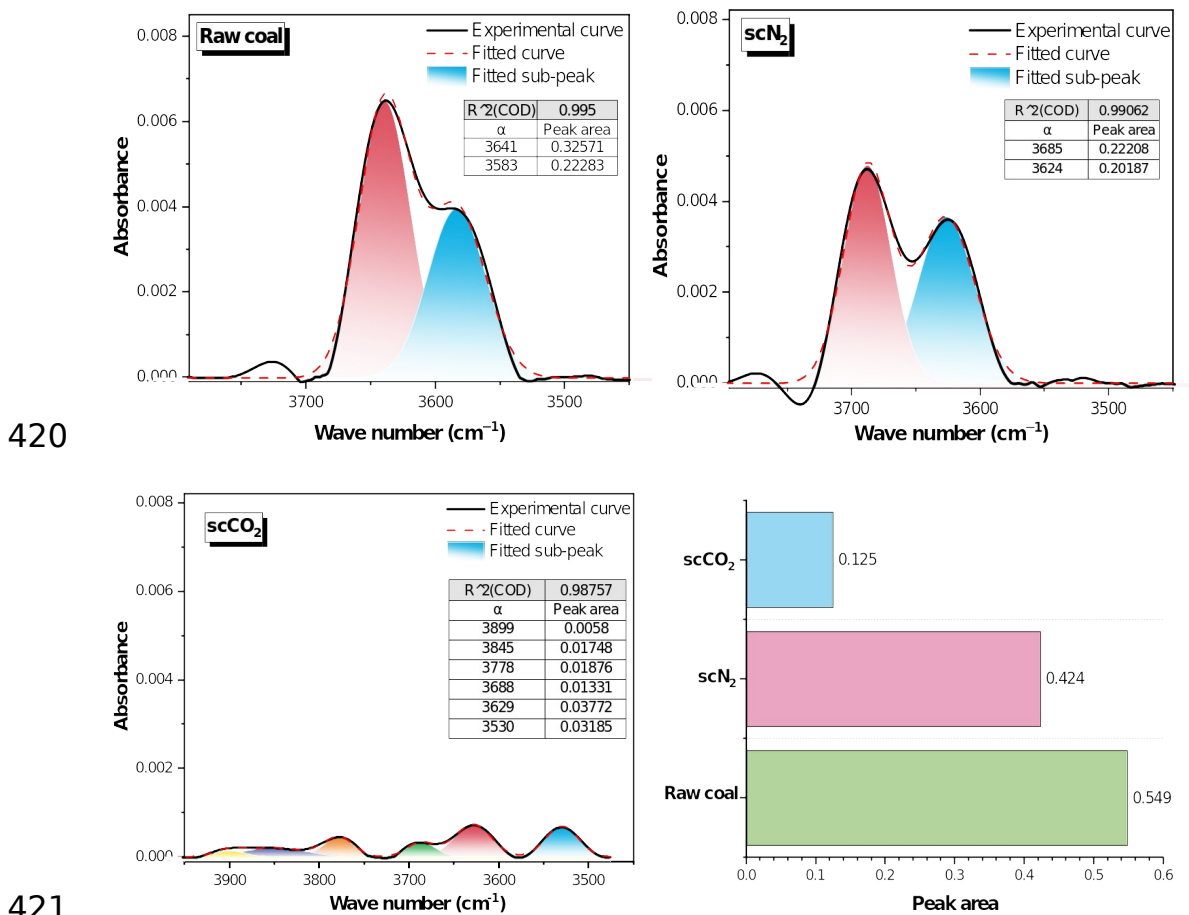
402

403 (1) Hydroxyl functional groups

404 The absorption peaks in the range of 3700–3200 cm^{-1} are mainly generated by
 405 stretching vibration of -OH, which is the main functional group for the formation of
 406 hydrogen bonds. As shown in **Figure 13**, absorption peaks appeared in the range of
 407 3650–3400 cm^{-1} , and main types of hydroxyl groups are OH- π , OH-OH, and
 408 free-OH.

409 The peak shape of coal for scCO_2 treatment was different from that of raw coal and
 410 coal for scN_2 treatment in **Figure 13**, and all of the sub-peak intensities of coal for

411 scCO₂ treatment were below 0.001. The integral areas of sub-peaks of hydroxyl groups
 412 for coal with H₂O treated by scCO₂, scN₂ and raw coal were 0.125, 0.424, and 0.549,
 413 respectively. The reduction of hydroxyl groups decreases the number of hydrogen
 414 bonds between H₂O molecules and C atoms of coal (Besford et al., 2020), whereas
 415 intermolecular forces (van der Waals) between CO₂ molecules and coal C atoms
 416 become prominent. Thus the adsorption potential of CO₂ on coal increases
 417 significantly (“Surface physical properties and its effects on the wetting behaviors of
 418 respirable coal mine dust,” 2013). Water films on the surface were displaced by CO₂
 419 dissolved in water, and water-wet surfaces changed to be intermediate-wet or CO₂-wet.



422 **Figure 13** Curve-fitting of FTIR spectra in the range of 3700–3200 cm⁻¹. α in the
 423 tables represent peak wave number, cm⁻¹. Peak areas from the different conditions are
 424 compared in the lower right bar graph.

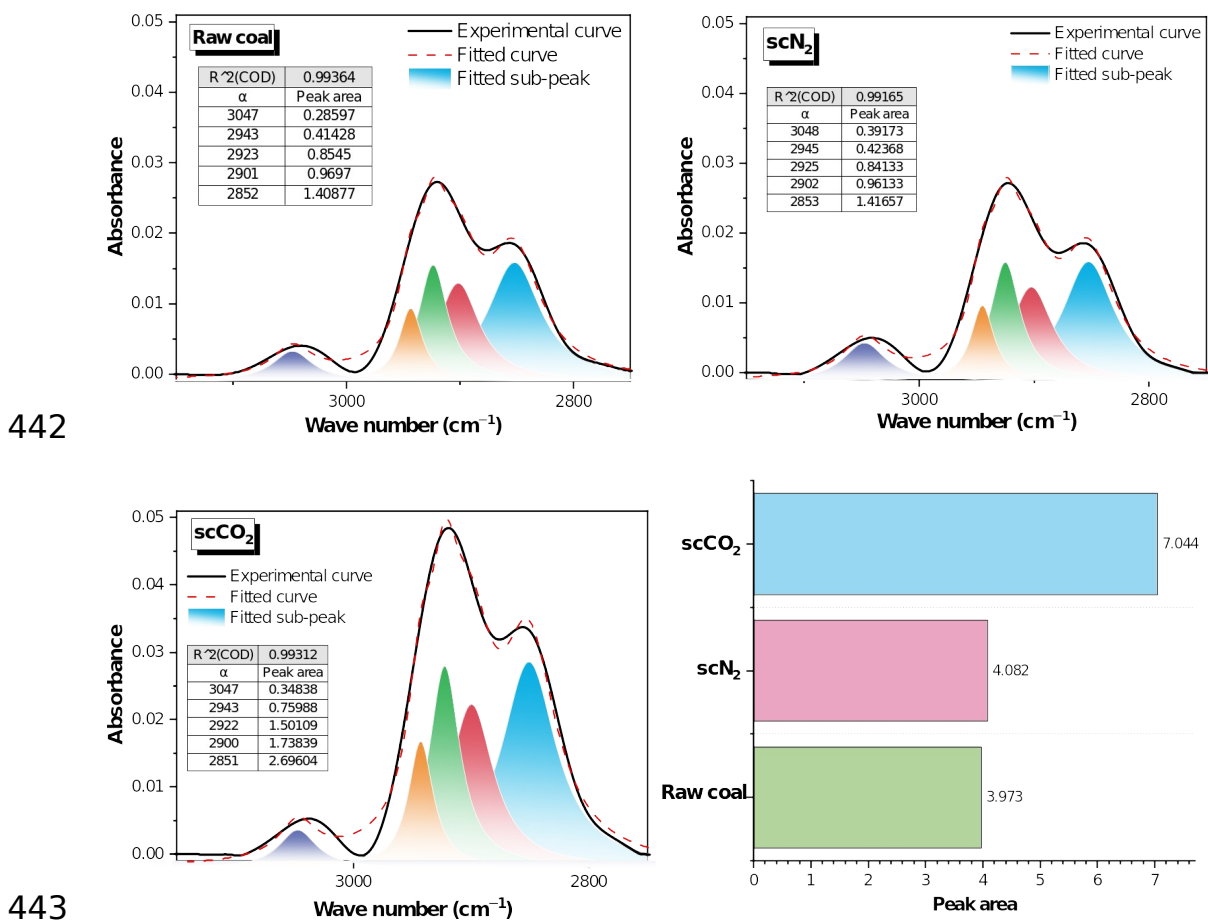
425

426 (2) Aliphatic hydrocarbons

427 In **Figure 14**, the absorption peaks in the range of 3000–2800 cm⁻¹ were mainly
 428 assigned to asymmetric vibrations of –CH₂ and –CH₃, and symmetric vibrations of
 429 –CH₂ and –CH₃. The peak positions of the above functional groups are located around
 430 2943 cm⁻¹, 2923 cm⁻¹, 2901 cm⁻¹ and 2852 cm⁻¹, respectively.

431 The integral areas of sub-peaks of aliphatic hydrocarbons for coal with H₂O treated
 432 by scCO₂, scN₂ and raw coal were 7.04, 4.08, 3.97, respectively. The increase of

433 aliphatic structure results from the alkylation of hydrocarbons under acidic conditions
 434 and implies an increase of the C atom ratio (Ni et al., 2019; Zhang et al., 2023). For
 435 scCO₂-H₂O treatment, the peak areas of the sub-peaks corresponding to -CH₃ and
 436 -CH₂ increased from 1.38 and 2.27 to 2.50 and 4.20, with -CH₂ having greater
 437 relative increase. A previous study (Guanhua et al., 2019) reported that wettability is
 438 positively correlated with the percentage area of -CH₃ and negatively correlated with
 439 -CH₂. This suggests that carbon content increased after the chemical reactions, and
 440 that increases in surface coverage with aliphatic hydrocarbons are detrimental to
 441 water-wetting.



443
 444 **Figure 14** Curve-fitting of FTIR spectra in the range of 3000–2800 cm⁻¹. α in the
 445 tables represent peak wave number, cm⁻¹. Peak areas from the different conditions are
 446 compared in the lower right bar graph.

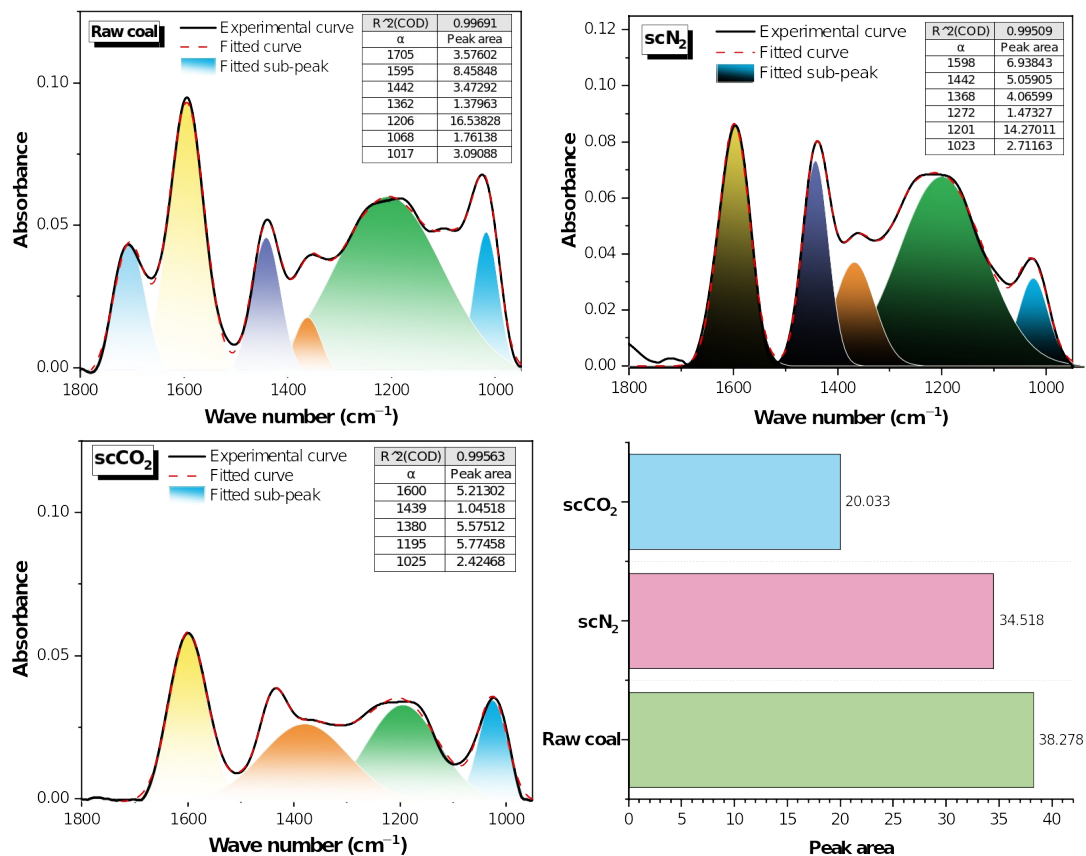
447
 448 (3) Oxygen-containing functional groups

449 As shown in **Figure 15**, the absorption peaks of oxygen-containing functional
 450 groups were mainly in the range of 1800-1000 cm⁻¹. The functional groups were
 451 assigned to COOH, aromatic nucleus C=C, symmetric -CH₃, C-O, C-O-C, which
 452 located near 1705 cm⁻¹, 1595 cm⁻¹, 1362 cm⁻¹, 1206 cm⁻¹, and 1068 cm⁻¹, respectively.

453 The integral areas of the sub-peaks of oxygen-containing functional groups for raw
 454 coal, coal with H₂O treated by scN₂, and coal with H₂O treated by sc CO₂ were 38.28,

455 34.52, and 20.33, respectively. The decrease of oxygen-containing functional groups
 456 after scCO₂ treatment reflects their shedding or dissociation on the surface (Boehm,
 457 1989). Oxygen-containing functional groups, including many polar components
 458 (Crawford et al., 1994), especially carboxyl groups, enhance interaction forces with
 459 polar molecules such as H₂O and are much stronger than the intermolecular forces
 460 (induced force and dispersion force) between CO₂ and oxygen-containing functional
 461 groups (Siemons et al., 2006). Therefore, it is difficult for CO₂ to displace H₂O
 462 molecules adsorbed directly on oxygen-containing functional groups at room-
 463 temperature and ambient-pressure (Gensterblum et al., 2014). Wu et al. similarly
 464 reported that reduction of oxygen-containing functional groups leads to weaker water-
 465 wetting as reflected in the shrinkage of precursor films and lower surface free energy
 466 (Wu et al., 2017). Shedding of polar oxygen-containing functional groups (especially
 467 carboxyl groups) after reactions with scCO₂ significantly weakened water-wetting.
 468

469



470

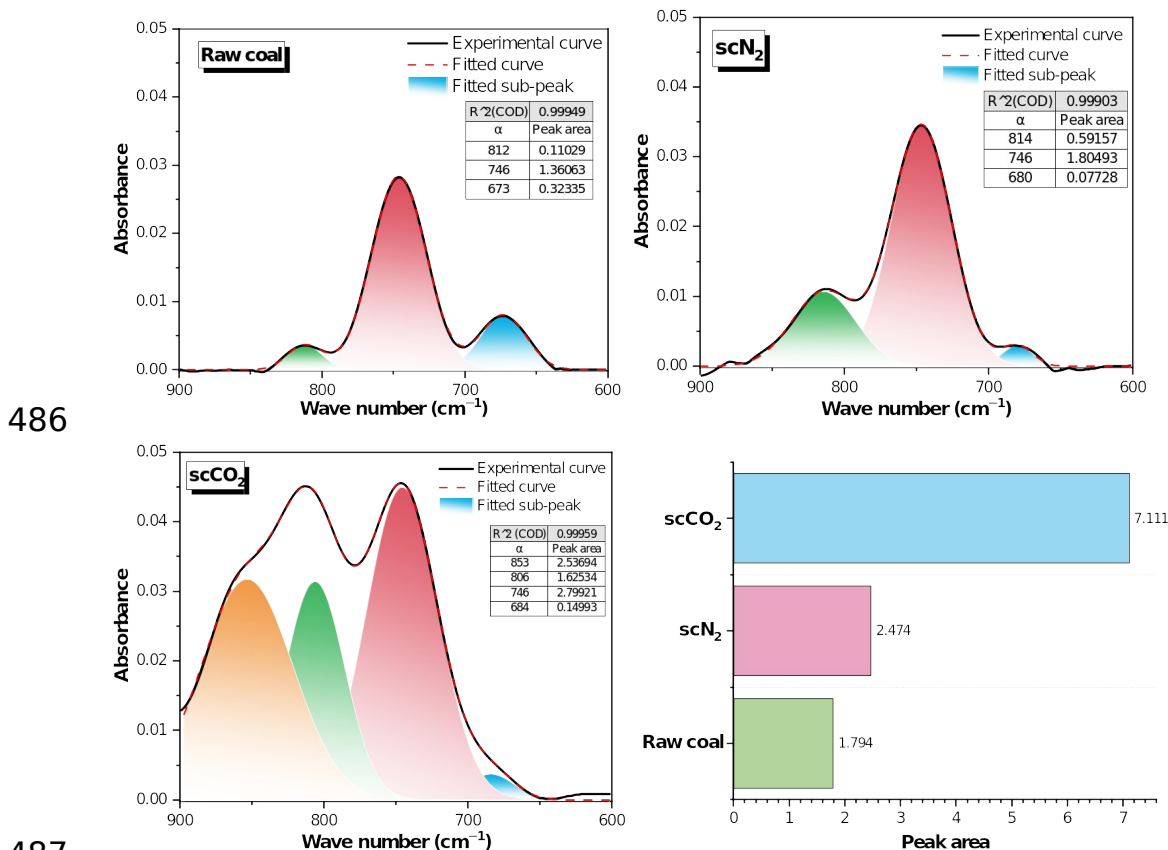
471 **Figure 15** Curve-fitting of FTIR spectra in the range of 1800–1000 cm⁻¹. α in the
 472 tables represent peak wave number, cm⁻¹. Peak areas from the different conditions are
 473 compared in the lower right bar graph.
 474

475 (4) Aromatic hydrocarbons

476 The adsorption peaks of waveband 900–600 cm⁻¹ in **Figure 16** mainly were
 477 assigned to the bending vibrations of substituted benzene rings. Compared with
 478 aliphatic hydrocarbons, most of aromatic hydrocarbons are also insoluble in water, but

479 the aromatic system is more stable.

480 The integral areas of the sub-peaks of aromatic hydrocarbons for raw coal, coal
481 treated by scN₂ and by scCO₂ were 1.79, 2.47, and 7.11, respectively. After scCO₂
482 treatment, the peak intensities and peak areas of two sub-peaks near 853 cm⁻¹, 806
483 cm⁻¹ increased significantly, which was attributed to the increase of aromatic structure
484 content (Wang et al., 2023) (main contribution), CO₃²⁻ ions, and silica (Fatah et al.,
485 2021b; Reig et al., 2002).



503 in 4.3 section.

504

505 **Table 3** Infrared structure parameters.

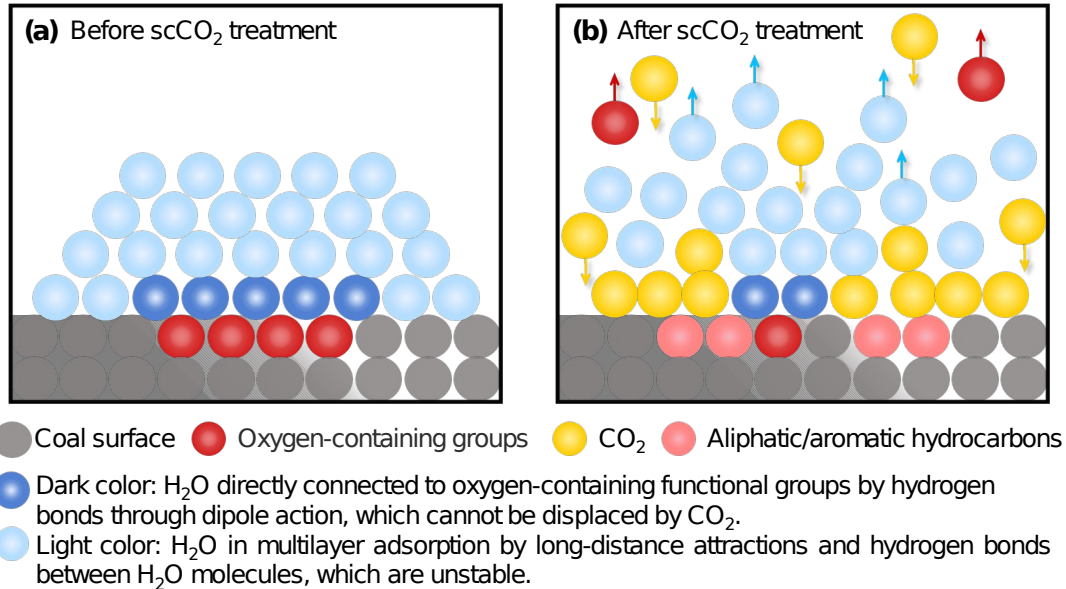
Structure parameter	Formula	Experimental group		
		scCO ₂	scN ₂	Raw coal
Aromaticity	$I = \frac{A_{900 \sim 700}}{A_{3000 \sim 2800}}$	1.279	0.775	0.563
Degree of aromatic ring condensation	$DOC = \frac{A_{CH_2} + A_{CH_3}}{A_{C=C}} = \frac{A_{900 \sim 700}}{A_{1605 \ 1595}}$	1.368	0.356	0.212
Length of aliphatic hydrocarbon chain	$A(CH_2)/A(CH_3) = \frac{A_{2920+2850}}{A_{2950+2870}}$	1.68	1.630	1.637

506

507 The overall impact of different treatments on surface chemistry is quantified by the
 508 average relative change of the absorption peak area ($\Delta' A$), given by

$$\Delta' A = \frac{1}{4} \sum_{i=1}^4 \frac{|A_{[scN_2]i} - A_{[raw\ coal]i}|}{A_{[raw\ coal]i}} \quad (6)$$

509 From this metric, changes in functional group content from scN₂-H₂O treatment were
 510 small relative to the original raw coal, *reflected* $\in a \Delta' A$ that is only 0.15 times that for
 511 the scCO₂-H₂O treatment. Such minor changes in surface chemistry imparted by
 512 exposure to scN₂, are consistent with small changes in measured contact angles. After
 513 scCO₂-H₂O treatment, the density of hydrophilic functional groups (hydroxyl and
 514 other polar oxygen-containing functional groups (Zhao et al., 2023)) decreased, while
 515 the hydrophobic functional groups (aromatic and aliphatic hydrocarbons (Xu et al.,
 516 2017)) increased. This tendency towards hydrophobicity results from three aspects: (1)
 517 the shedding of polar oxygen-containing functional groups, (2) the reduction of
 518 hydrogen bonds, (3) elevated coal rank and the increased percentage of surface
 519 hydrocarbons. Fewer sites of polar oxygen-containing functional groups were available
 520 for H₂O directly adsorbing (dark color in **Figure 17** (b)). The intermolecular force
 521 (hydrogen bonds between H₂O) and long-distance attractions weakened so that H₂O in
 522 multilayer adsorption (light color) was displaced or washed away by CO₂. Coal
 523 surfaces with a higher percentage of hydrocarbons and a tendency to be graphitized
 524 are more hydrophobic and more capable of CO₂ adsorption.



525

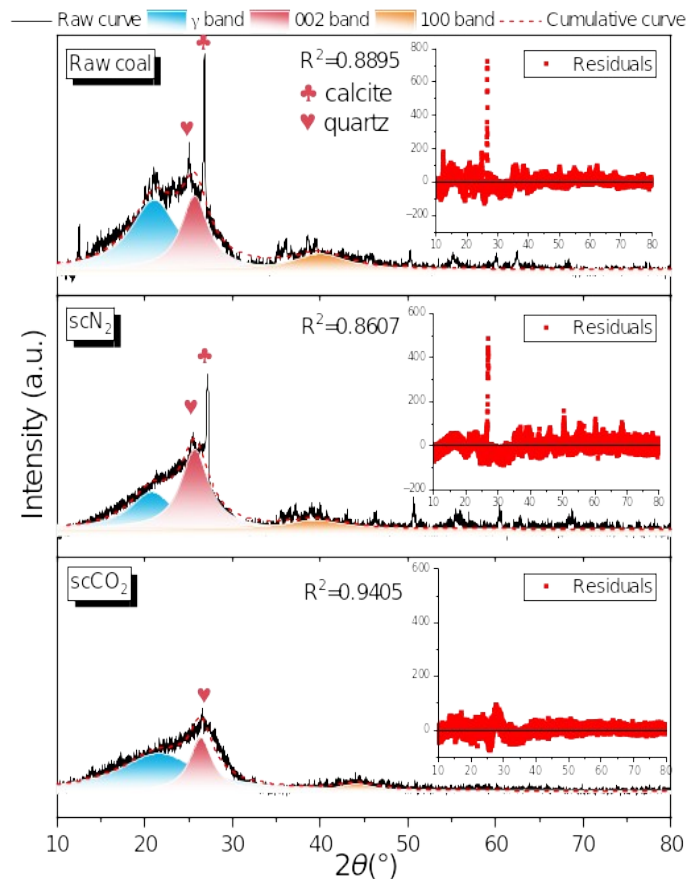
526 **Figure 17** Schematic diagram of the effect of CO₂ adsorption and functional group
 527 alterations on wettability.

528

529 4.3 Coal crystallite structure

530 XRD patterns of coal generally have two diffraction peaks (002- and 100-peak)
 531 corresponding to diffraction angles (2θ) $\sim 26^\circ$ and 44° , respectively. The asymmetry of
 532 diffraction peak (raw curve in **Figure 18**) is caused by the γ -band related to saturated
 533 structures like aliphatic chains or aliphatic rings (Kamble et al., 2022). The 002-peak
 534 was distinct while the 100-peak was not, as shown in **Figure 18**, indicating that the
 535 main crystalline phase is carbon.

536 In general, the intensity of the diffraction peak decreased after scCO₂ treatment,
 537 indicating that mineral content decreased, especially calcite (club label near $2\theta \sim 30^\circ$ in
 538 **Figure 18**), and only the diffraction peak of quartz (heart label) was still clearly
 539 present. As shown in **Figure 18**, residual analysis showed that conventional residuals
 540 at the peak position of calcite deviated clearly from mode-fitting values of cumulative
 541 curve. The diffraction peak of calcite was the reason for coefficient of determination
 542 $R^2 < 0.90$ in raw coal and scN₂ treatment. A previous study eliminated this strong peak
 543 in coal by acid leaching (Yan et al., 2020), causing the decomposition of calcite in
 544 carbonic acid as described by Eqs. (2).



545

546 **Figure 18** Curve-fitting of XRD patterns and residual analysis. The mineral labeling
 547 was accomplished through comparisons with standard cards in Jade and with previous
 548 work (Tian et al., 2017; Yan et al., 2020).

549

550 Crystallite structure parameters in **Table 4** were calculated with the Bragg's and
 551 Scherrer's formulae (7)–(11) (Matlala et al., 2021): aromatic interlayer spacing d_{002} ,
 552 crystallite diameter L_a , crystallite height L_c , the number of aromatic stacking layers N ,
 553 and coalification degree D . Full width at half maximums (FWHM) and peak mean
 554 centers of 002- and 100-peak used to calculate crystallite parameters were obtained
 555 from the fitting results shown in **Table A.2**.

556 The d_{002} for raw coal, scN₂ treatment, and scCO₂ treatment were 3.46 Å, 3.46 Å,
 557 3.37 Å, respectively, and the reduction of interlayer spacing implied closer
 558 arrangement of aromatic layer structure. For scCO₂ treatment, the diffraction angle of
 559 002-peak was 26.4° and close to that of pure graphite (26.6°). L_a , L_c , and N both
 560 increased, indicating the degree of molecular polymerization and the size of carbon
 561 crystalline developed (Sonibare et al., 2010). The D for raw coal, scN₂ treatment, and
 562 scCO₂ treatment were 82.3%, 82.6%, and 97.1%, respectively. From the XRD patten
 563 of the scCO₂ treated coal, we find that inorganic mineral abundance reduced, and
 564 carbon crystallites tended to graphite-like structure: the crystallite growth and the
 565 higher degree of long-range ordering in aromatic carbon (Zhang et al., 2021). These
 566 changes to crystallite structure are usually detrimental for water-wetting because of the

567 higher carbon content and the lower negative surface charge after structure
 568 development (Fuerstenau et al., 1988). Moreover, crystallite development usually is
 569 associated with elevated coal rank, which is positively correlated with contact angle
 570 (Shojai Kaveh et al., 2012; Yan et al., 2015).

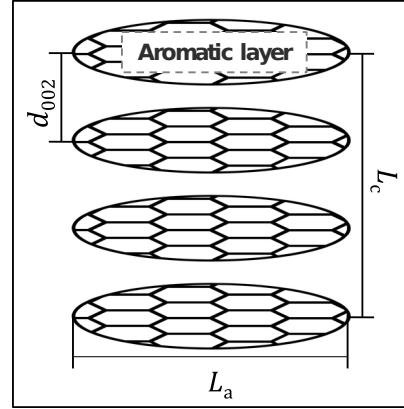
$$d_{002} = \frac{\lambda}{2 \sin \theta_{002}} \quad (7)$$

$$L_a = \frac{K_1 \lambda}{\beta_{(100)} \cos \theta_{(100)}} \quad (8)$$

$$L_c = \frac{K_2 \lambda}{\beta_{(002)} \cos \theta_{(002)}} \quad (9)$$

$$N = \frac{L_c}{d_{002}} + 1 \quad (10)$$

$$D = \frac{d_{CE} - d_{002}}{d_{CE} - d_{GR}} \times 100\% \quad (11)$$



571 where λ is the X-ray wavelength, the copper target is taken as 1.54056 Å; $\theta_{(002)}$, $\theta_{(100)}$
 572 are the Bragg angles of the 002 and 100 diffraction peaks, respectively, (°); $\beta_{(002)}$, $\beta_{(100)}$
 573 are the half-height widths of the 002 and 100 diffraction peaks, respectively, (rad); K_1 ,
 574 K_2 are Debye-Scherrer constants and crystallite shape factors. K_1 , K_2 are taken as
 575 1.84, 0.94, respectively. d_{CE} and d_{GR} are cellulose of $d_{002} = 3.975$ Å and graphite
 576 of $d_{002} = 3.354$ Å, respectively.

577

578 **Table 4** Crystallite structure parameters.

Coal sample	$d_{002}/\text{Å nm}$	$L_a/\text{Å}$	$L_c/\text{Å}$	N	$D/\%$
Raw coal	3.46	25.69	23.80	7.87	82.28%
N ₂	3.46	21.93	20.84	7.02	82.61%
CO ₂	3.37	37.64	26.16	8.76	97.08%

579

580

581

582

583

584 5 Implications

585 In this study, the interaction of CO₂-H₂O-coal systems were shown to change coal
 586 surfaces from water-wetting to intermediate-wetting. This determines the pore-scale
 587 configuration of fluids and fluid flow, thereby affecting reservoir-scale fluid dynamics.

588 After CO₂ treatment, hvBb coal in the situ reservoir condition ($P=120$ bar, $T=45^{\circ}\text{C}$) is
 589 favorable for CO₂-ECBM projects. In this case, reduced capillary forces favor CO₂
 590 injection and percolation rate in coal seams (Sakurovs and Lavrencic, 2011; Arif et al.,
 591 2016b), resulting in a wider and more homogeneous distribution of CO₂. CO₂
 592 displacement efficiency is evaluated by capillary number N_{ca} , where larger contact
 593 angles makes N_{ca} larger, i.e., water or methane is more easily displaced (Shojai Kaveh
 594 et al., 2011).

$$N_{ca} = \frac{\mu \times v}{\gamma_{lg} \times \cos\theta} \quad (12)$$

595 The wetting phase transition is also favorable for overcoming the water blocking
 596 effect (water as the wetting phase blocks the methane in the micropores) that affects
 597 hydraulic fracturing (Li et al., 2022). CO₂, as the wetting phase, can enter the
 598 micropores and displace methane due to its stronger adsorption capacity (Pini et al.,
 599 2010).

600 However, this alteration also imparts a detrimental impact on CO₂ sequestration
 601 because storage capacity under caprock is limited by the balance between capillary
 602 force and buoyancy. This balance limits the permanently immobilized CO₂ storage
 603 height h (Iglauer, 2018)

$$\begin{cases} P_c \leq \frac{2\gamma\cos\theta}{r} \\ P_b = \Delta\rho g h \end{cases} \implies h = \frac{2\gamma\cos\theta}{\Delta\rho g r} \quad (13)$$

604 Increasing contact angles indicate the decrease in storage capacity and containment
 605 security. The advancing and receding contact angles measured in this study reflect
 606 fluid migration processes such as displacement and flowback, and can be utilized to
 607 predict and improve field practices, including nanoparticles, surfactants, and polymers
 608 used to modify wettability (Ali et al., 2023).
 609

610 **6 Conclusions**

611 We measured time-dependent dynamic and static contact angles (CA) on coal
 612 surfaces exposed to CO₂/N₂- H₂O using the captive bubble method, with the
 613 nonaqueous phase in gaseous and supercritical states. We characterized
 614 physicochemical properties by FTIR, XRD, and SEM in order to identify the
 615 mechanisms responsible for weakening water-wetting after scCO₂ treatment. The main
 616 conclusions are as follows.

617 (1) The contact angles (CAs) for gas and supercritical N₂ treatment only changed
 618 slightly. For gaseous CO₂ treatment, the dynamic CA also varied slightly. For scCO₂
 619 treatment, both the static and dynamic CAs increased significantly, and the average θ_{adv}
 620 changed from water-wet (27° for scN₂ treatment) to intermediate-wet (92°).

621 (2) The chemical reactions of minerals resulted in inhomogeneous and rougher
 622 surfaces with corrosion pores, connecting partially isolated pores, fracture extension,
 623 and edge warping, finally generating greater contact angle hysteresis; all which favor

624 CO₂-wetting.

625 (3) The abundance of hydrophilic functional groups decreased while that of
626 hydrophobic functional groups increased following scCO₂ treatment. The unfavorable
627 water-wet changes were reflected in four aspects: the shedding of polar oxygen-
628 containing functional groups, the reduction of hydrogen bonds, elevated coal rank, and
629 increased percentage of hydrocarbons.

630 (4) scCO₂ treatment depleted most of the inorganic mineral components (most
631 notably calcite). The molecular polymerization of carbon was higher and crystallites
632 developed toward graphite-like growth and elevated coal rank. These changes in
633 crystallite structure are not favorable for water-wetting due to the higher carbon
634 content and lower surface charge.

635

636 CRediT authorship contribution statement

637 **Ke Li:** Investigation, Writing–original draft, Formal analysis, Visualization.
638 **Chuanjie Zhu:** Writing–review & editing, Methodology, Funding acquisition,
639 Supervision. **Jiamin Wan:** Writing–review & editing, Conceptualization,
640 Supervision, Resources. **Tetsu K. Tokunaga:** Writing–review & editing,
641 Supervision. **Na Liu:** Investigation. **Cong Ma:** Investigation. **Baiquan Lin:** Project
642 administration.

643 Declaration of competing interest

644 The authors declare that they have no known competing financial interests or personal
645 relationships that could have appeared to influence the work reported in this paper.

646 Acknowledgements

647 This work was supported by the National Natural Science Foundation of China
648 (NSFC) (Grant Number: 52174211); the National Science and Technology Major
649 Project (Grant Number: 2020YFA0711803); and the Key Program of the National
650 Natural Science Foundation of China (Grant Number: 52334007). This material is
651 also partly based upon work supported by the U.S. Department of Energy, Office of
652 Fossil Energy, Office of Natural Gas and Petroleum Technology, through the National
653 Energy Technology Laboratory, under Award Number DE-AC02-05CH11231.

654 Data availability

655 Data will be made available on request.

656 References

- 657 Ali, Muhammad, Yekeen, N., Ali, Mujahid, Hosseini, M., Pal, N., Keshavarz, A.,
658 Iglauer, S., Hoteit, H., 2022. Effects of Various Solvents on Adsorption of
659 Organics for Porous and Nonporous Quartz/CO₂/Brine Systems: Implications for
660 CO₂ Geo-Storage. *Energy Fuels* 36, 11089–11099. <https://doi.org/10/gst85h>
- 661 Ao, X., Lu, Y., Tang, J., Chen, Y., Li, H., 2017. Investigation on the physics structure
662 and chemical properties of the shale treated by supercritical CO₂. *Journal of CO₂*
663 *Utilization* 20, 274–281. <https://doi.org/10/gbqwqq>
- 664 Arain, Z.-U.-A., Aftab, A., Ali, M., Altaf, M., Sarmadivaleh, M., 2023. Influence of
665 stearic acid and alumina nanofluid on CO₂ wettability of calcite substrates:
666 Implications for CO₂ geological storage in carbonate reservoirs. *Journal of*
667 *Colloid and Interface Science* 646, 567–575. <https://doi.org/10/gst849>
- 668 Arif, M., Al-Yaseri, A.Z., Barifcani, A., Lebedev, M., Iglauer, S., 2016a. Impact of
669 pressure and temperature on CO₂–brine–mica contact angles and CO₂–brine
670 interfacial tension: Implications for carbon geo-sequestration. *Journal of Colloid*
671 *and Interface Science* 462, 208–215. <https://doi.org/10/gst85c>
- 672 Arif, M., Barifcani, A., Lebedev, M., Iglauer, S., 2016b. CO₂-wettability of low to
673 high rank coal seams: Implications for carbon sequestration and enhanced
674 methane recovery. *Fuel* 181, 680–689. <https://doi.org/10.1016/j.fuel.2016.05.053>
- 675 Battino, R., Rettich, T.R., Tominaga, T., 1984. The Solubility of Nitrogen and Air in
676 Liquids. *Journal of Physical and Chemical Reference Data - J PHYS CHEM REF*
677 *DATA* 13, 563–600. <https://doi.org/10/fs6ghq>
- 678 Besford, Q.A., Christofferson, A.J., Kalayan, J., Sommer, J.-U., Henchman, R.H.,
679 2020. The Attraction of Water for Itself at Hydrophobic Quartz Interfaces. *J.*
680 *Phys. Chem. B* 124, 6369–6375. <https://doi.org/10/gst84t>
- 681 Bhutani, G., Khandekar, S., Muralidhar, K., 2012. CONTACT ANGLES OF
682 PENDANT DROPS ON ROUGH SURFACES.
- 683 Boehm, H.P., 1989. Surface Properties of Carbons, in: Morterra, C., Zecchina, A.,
684 Costa, G. (Eds.), *Studies in Surface Science and Catalysis, Structure and*
685 *Reactivity of Surfaces*. Elsevier, pp. 145–157. [https://doi.org/10.1016/S0167-](https://doi.org/10.1016/S0167-2991(08)60678-3)
686 [2991\(08\)60678-3](https://doi.org/10.1016/S0167-2991(08)60678-3)
- 687 Cai, Z., Song, Y., 2021. Implementing Contact Angle Hysteresis in Moving Mesh-
688 Based Two-Phase Flow Numerical Simulations. *ACS Omega* 6, 35711–35717.
689 <https://doi.org/10/gst84w>
- 690 Chaturvedi, T., Schembre, J.M., Kovscek, A.R., 2009. Spontaneous imbibition and
691 wettability characteristics of Powder River Basin coal. *International Journal of*
692 *Coal Geology, CO₂ Sequestration in Coals and Enhanced Coalbed Methane*
693 *Recovery* 77, 34–42. <https://doi.org/10.1016/j.coal.2008.08.002>

694 Chau, T.T., 2009. A review of techniques for measurement of contact angles and their
695 applicability on mineral surfaces. *Minerals Engineering* 22, 213–219.
696 <https://doi.org/10.1016/j.mineng.2008.07.009>

697 Chen, C., Wan, J., Li, W., Song, Y., 2015. Water contact angles on quartz surfaces
698 under supercritical CO₂ sequestration conditions: Experimental and molecular
699 dynamics simulation studies. *International Journal of Greenhouse Gas Control*
700 42, 655–665. <https://doi.org/10.1016/j.ijggc.2015.09.019>

701 Chen, Y., Ma, D., Xia, Y., Guo, C., Yang, F., Shao, K., 2019. Study on wettability and
702 influencing factors of different macroscopic components in low rank coal. *Coal*
703 *Science and Technology* 47, 97–104.
704 <https://doi.org/10.13199/j.cnki.cst.2019.09.009>

705 Crawford, R., Guy, D., Mainwaring, D., 1994. The influence of coal rank and mineral
706 matter content on contact angle hysteresis. *Fuel* 73, 742–746.
707 [https://doi.org/10.1016/0016-2361\(94\)90018-3](https://doi.org/10.1016/0016-2361(94)90018-3)

708 Drelich, J., 2013. Guidelines to measurements of reproducible contact angles using a
709 sessile-drop technique. *Surface Innovations* 1, 248–254.
710 <https://doi.org/10.1680/si.13.00010>

711 Fatah, A., Bennour, Z., Mahmud, H.B., Gholami, R., Hossain, M., 2021a. Surface
712 wettability alteration of shales exposed to CO₂: Implication for long-term
713 integrity of geological storage sites. *International Journal of Greenhouse Gas*
714 *Control* 110, 103426. <https://doi.org/10/gst846>

715 Fatah, A., Mahmud, H.B., Bennour, Z., Hossain, M., Gholami, R., 2021b. Effect of
716 supercritical CO₂ treatment on physical properties and functional groups of
717 shales. *Fuel* 303, 121310. <https://doi.org/10/gst84n>

718 Fuerstenau, D.W., Rosenbaum, J.M., You, Y.S., 1988. Electrokinetic behavior of coal.
719 *Energy Fuels* 2, 241–245. <https://doi.org/10/b6fmr7>

720 Gathitu, B.B., Chen, W.Y., McClure, M., 2009. Effects of coal interaction with
721 supercritical CO₂: physical structure. *Industrial and Engineering*
722 *Chemistry Research* 48. <https://doi.org/10/fw7mfg>

723 Gensterblum, Y., Busch, A., Krooss, B.M., 2014. Molecular concept and experimental
724 evidence of competitive adsorption of H₂O, CO₂ and CH₄ on organic material.
725 *Fuel* 115, 581–588. <https://doi.org/10.1016/j.fuel.2013.07.014>

726 Godoi, J.M., Matai, P., 2021. Enhanced oil recovery with carbon dioxide
727 geosequestration: first steps at Pre-salt in Brazil. *Journal of Petroleum*
728 *Exploration and Production Technology* 11, 1429–1441.
729 <https://doi.org/10.1007/s13202-021-01102-8>

730 Guanhua, N., Qian, S., Meng, X., Hui, W., Yuhang, X., Weimin, C., Gang, W., 2019.
731 Effect of NaCl-SDS compound solution on the wettability and functional groups
732 of coal. *Fuel* 257, 116077. <https://doi.org/10.1016/j.fuel.2019.116077>

733 Hadi Mosleh, M., Sedighi, M., Vardon, P.J., Turner, M., 2017. Efficiency of Carbon
734 Dioxide Storage and Enhanced Methane Recovery in a High Rank Coal. *Energy*
735 *Fuels* 31, 13892–13900. <https://doi.org/10.1021/acs.energyfuels.7b02402>

- 736 Ibrahim, A.F., Nasr-El-Din, H.A., 2016. Effect of Water Salinity on Coal Wettability
737 During CO₂ Sequestration in Coal Seams. *Energy Fuels* 30, 7532–7542.
738 <https://doi.org/10/f85s3x>
- 739 Iglauer, S., 2011. Dissolution Trapping of Carbon Dioxide in Reservoir Formation
740 Brine – A Carbon Storage Mechanism. <https://doi.org/10.5772/20206>
- 741 Iglauer, S., Mathew, M.S., Bresme, F., 2012. Molecular dynamics computations of
742 brine–CO₂ interfacial tensions and brine–CO₂–quartz contact angles and their
743 effects on structural and residual trapping mechanisms in carbon geo-
744 sequestration. *Journal of Colloid and Interface Science* 386, 405–414.
745 <https://doi.org/10.1016/j.jcis.2012.06.052>
- 746 Jia, Q., Liu, D., Cai, Y., Lu, Y., Li, R., Wu, H., Zhou, Y., 2022. Nano-CT
747 measurement of pore-fracture evolution and diffusion transport induced by
748 fracturing in medium-high rank coal. *Journal of Natural Gas Science and*
749 *Engineering* 106. <https://doi.org/10/gst84s>
- 750 Jung, J.-W., Wan, J., 2012. Supercritical CO₂ and Ionic Strength Effects on Wettability
751 of Silica Surfaces: Equilibrium Contact Angle Measurements. *Energy Fuels* 26,
752 6053–6059. <https://doi.org/10/f4bn9d>
- 753 Kamble, A.D., Mendhe, V.A., Chavan, P.D., Saxena, V.K., 2022. Insights of mineral
754 catalytic effects of high ash coal on carbon conversion in fluidized bed Co-
755 gasification through FTIR, XRD, XRF and FE-SEM. *Renewable Energy* 183,
756 729–751. <https://doi.org/10.1016/j.renene.2021.11.022>
- 757 Kulinich, S.A., Farzaneh, M., 2009. Effect of contact angle hysteresis on water droplet
758 evaporation from super-hydrophobic surfaces. *Applied Surface Science* 255,
759 4056–4060. <https://doi.org/10.1016/j.apsusc.2008.10.109>
- 760 Labus, K., Bujok, P., 2011. CO₂ mineral sequestration mechanisms and capacity of
761 saline aquifers of the Upper Silesian Coal Basin (Central Europe) - Modeling and
762 experimental verification. *Energy, PRES 2010* 36, 4974–4982. <https://doi.org/10/cqqgsn>
- 763
- 764 Lerman, A., Mackenzie, F.T., 2018. Carbonate Minerals and the CO₂-Carbonic Acid
765 System, in: White, W.M. (Ed.), *Encyclopedia of Geochemistry: A Comprehensive*
766 *Reference Source on the Chemistry of the Earth, Encyclopedia of Earth Sciences*
767 *Series*. Springer International Publishing, Cham, pp. 206–226.
768 https://doi.org/10.1007/978-3-319-39312-4_84
- 769 Li, K., Zhu, C., Liu, S., Chen, D., Cai, G., 2022. Effects of Injection Pressure and
770 Duration on Alternate High-Pressure Water-Gas Sequestration of Coalbed
771 Methane. *Geofluids* 2022, 1–15. <https://doi.org/10.1155/2022/4563438>
- 772 Liu, S., Yang, X., Qin, Y., 2010. Molecular dynamics simulation of wetting behavior at
773 CO₂/water/solid interfaces. *Chinese Science Bulletin* 55, 2252–2257.
774 <https://doi.org/10/cs2cjj>
- 775 Liu, S., Zhu, C., Li, Y., Hu, S., Zhang, X., Ma, C., 2023. Mechanism of adsorption
776 capacity enhancement of coal due to interaction with high-pressure scCO₂-water
777 system. *Gas Science and Engineering* 117, 205080.

778 <https://doi.org/10.1016/j.jgsce.2023.205080>

779 Liu, X., Sang, S., Zhou, X., Wang, Z., 2023. Coupled adsorption-hydro-thermo-
780 mechanical-chemical modeling for CO₂ sequestration and well production during
781 CO₂-ECBM. *Energy* 262, 125306. <https://doi.org/10.1016/j.energy.2022.125306>

782 Lu, Y., Tian, R., Liu, W., Tang, J., Li, H., Chen, X., Sun, X., 2021. Mechanisms of
783 shale water wettability alteration with chemical groups after CO₂ injection:
784 Implication for shale gas recovery and CO₂ geo-storage. *Journal of Natural Gas
785 Science and Engineering* 90, 103922. <https://doi.org/10/gst84m>

786 MacInnes, D.A., Belcher, D., 1933. The Thermodynamic Ionization Constants of
787 Carbonic Acid. *J. Am. Chem. Soc.* 55, 2630–2646.
788 <https://doi.org/10.1021/ja01334a003>

789 Matlala, I.V., Moroeng, O.M., Wagner, N.J., 2021. Macromolecular structural changes
790 in contact metamorphosed inertinite-rich coals from the No. 2 Seam, Witbank
791 Coalfield (South Africa): Insights from petrography, NMR and XRD.
792 *International Journal of Coal Geology* 247, 103857.
793 <https://doi.org/10.1016/j.coal.2021.103857>

794 Ni, G., Li, Z., Sun, Q., Li, S., Dong, K., 2019. Effects of [Bmim][Cl] ionic liquid with
795 different concentrations on the functional groups and wettability of coal.
796 *Advanced Powder Technology* 30, 610–624.
797 <https://doi.org/10.1016/j.appt.2018.12.008>

798 Pini, R., Ottiger, S., Storti, G., Mazzotti, M., 2010. Prediction of competitive
799 adsorption on coal by a lattice DFT model. *Adsorption* 16, 37–46. <https://doi.org/10.1007/s10450-009-9197-2>

800

801 Reig, F.B., Adelantado, J.V.G., Moya Moreno, M.C.M., 2002. FTIR quantitative
802 analysis of calcium carbonate (calcite) and silica (quartz) mixtures using the
803 constant ratio method. Application to geological samples. *Talanta* 58, 811–821.
804 <https://doi.org/10/b5g7j2>

805 Roshan, H., Al-Yaseri, A.Z., Sarmadivaleh, M., Iglauer, S., 2016. On wettability of
806 shale rocks. *Journal of Colloid and Interface Science* 475, 104–111.
807 <https://doi.org/10/f8qd6k>

808 Sabirzyanov, A.N., Il'in, A.P., Akhunov, A.R., Gumerov, F.M., 2002. Solubility of
809 Water in Supercritical Carbon Dioxide 40.

810 Shang, L., Guanhua, N., Baisheng, N., Shouqing, L., Xijian, L., Gang, W., 2021.
811 Microstructure characteristics of lignite under the synergistic effect of oxidizing
812 acid and ionic liquid [Bmim][Cl]. *Fuel* 289, 119940.
813 <https://doi.org/10.1016/j.fuel.2020.119940>

814 Shojai Kaveh, N., Barnhoorn, A., Wolf, K.-H., 2016. Wettability evaluation of silty
815 shale caprocks for CO₂ storage. *International Journal of Greenhouse Gas Control*
816 49, 425–435. <https://doi.org/10/f8pftv>

817 Shojai Kaveh, N., Rudolph, E.S.J., Wolf, K.-H.A.A., Ashrafizadeh, S.N., 2011.
818 Wettability determination by contact angle measurements: hvbB coal–water
819 system with injection of synthetic flue gas and CO₂. *Journal of Colloid and*

820 Interface Science 364, 237–247. <https://doi.org/10.1016/j.jcis.2011.07.091>

821 Shojai Kaveh, N., Wolf, K.-H., Ashrafizadeh, S.N., Rudolph, E.S.J., 2012. Effect of
822 coal petrology and pressure on wetting properties of wet coal for CO₂ and flue
823 gas storage. *International Journal of Greenhouse Gas Control*, CATO: CCS
824 Research in the Netherlands 11, S91–S101.
825 <https://doi.org/10.1016/j.ijggc.2012.09.009>

826 Siemons, N., Bruining, H., Castelijn, H., Wolf, K.-H., 2006. Pressure dependence of
827 the contact angle in a CO₂–H₂O–coal system. *Journal of Colloid and Interface
828 Science* 297, 755–761. <https://doi.org/10/brm7zc>

829 Sonibare, O., Haeger, T., Foley, S., 2010. Structural characterization of Nigerian coals
830 by X-ray diffraction, Raman and FTIR spectroscopy. *Energy* 35, 5347–5353.
831 <https://doi.org/10.1016/j.energy.2010.07.025>

832 Sun, E.W.-H., Bourg, I.C., 2023. Impact of organic solutes on capillary phenomena in
833 water-CO₂-quartz systems. *Journal of Colloid and Interface Science* 629, 265–
834 275. <https://doi.org/10.1016/j.jcis.2022.08.124>

835 Sun, X., Yao, Y., Liu, D., Elsworth, D., 2022. How Does CO₂ Adsorption Alter Coal
836 Wettability? Implications for CO₂ Geo-Sequestration. *Journal of Geophysical
837 Research: Solid Earth* 127, e2021JB023723. <https://doi.org/10/gqdg8j>

838 Surface physical properties and its effects on the wetting behaviors of respirable coal
839 mine dust, 2013. *Powder Technology* 233, 137–145. <https://doi.org/10/gnmxwz>

840 Tenney, C.M., Cygan, R.T., 2014. Molecular Simulation of Carbon Dioxide, Brine,
841 and Clay Mineral Interactions and Determination of Contact Angles. *Environ.
842 Sci. Technol.* 48, 2035–2042. <https://doi.org/10/f5sdx>

843 Tian, B., Qiao, Y., Fan, J., Bai, L., Tian, Y., 2017. Coupling Pyrolysis and Gasification
844 Processes for Methane-Rich Syngas Production: Fundamental Studies on
845 Pyrolysis Behavior and Kinetics of a Calcium-Rich High-Volatile Bituminous
846 Coal. *Energy Fuels* 31, 10665–10673.
847 <https://doi.org/10.1021/acs.energyfuels.7b01788>

848 Tokunaga, T.K., 2012. DLVO-Based Estimates of Adsorbed Water Film Thicknesses
849 in Geologic CO₂ Reservoirs. *Langmuir* 28, 8001–8009.
850 <https://doi.org/10/f3z83w>

851 Tokunaga, T.K., Wan, J., Jung, J.-W., Kim, T.W., Kim, Y., Dong, W., 2013. Capillary
852 pressure and saturation relations for supercritical CO₂ and brine in sand: High-
853 pressure Pc(Sw) controller/meter measurements and capillary scaling predictions.
854 *Water Resources Research* 49, 4566–4579. <https://doi.org/10.1002/wrcr.20316>

855 Wan, J., Kim, Y., Tokunaga, T.K., 2014. Contact angle measurement ambiguity in
856 supercritical CO₂–water–mineral systems: Mica as an example. *International
857 Journal of Greenhouse Gas Control* 31, 128–137.
858 <https://doi.org/10.1016/j.ijggc.2014.09.029>

859 Wang, D.-B., Zhou, F.-J., Li, Y.-P., Yu, B., Martyushev, D., Liu, X.-F., Wang, M., He,
860 C.-M., Han, D.-X., Sun, D.-L., 2022. Numerical simulation of fracture
861 propagation in Russia carbonate reservoirs during refracturing. *Petroleum Science*

862 19, 2781–2795. <https://doi.org/10/gst84r>

863 Wang, H., Zhang, L., Wang, D., He, X., 2017. Experimental investigation on the
864 wettability of respirable coal dust based on infrared spectroscopy and contact
865 angle analysis. *Advanced Powder Technology* 28, 3130–3139.
866 <https://doi.org/10.1016/j.appt.2017.09.018>

867 Wang, Z., Wang, G., Hao, C., Ni, G., Zhao, W., Cheng, Y., Wang, L., 2023. Chemical
868 structure and hydrocarbon generation characteristics of tectonic coal with
869 different metamorphic degrees: Implications for gas adsorption capacity. *Gas
870 Science and Engineering* 112, 204949.
871 <https://doi.org/10.1016/j.gjsce.2023.204949>

872 Wei, J., Wang, H., Si, L., Xi, Y., 2022. Characteristics of coal-water solid-liquid
873 contact in gas atmosphere. *Journal of China Coal Society* 47, 323–332.
874 <https://doi.org/10.13225/j.cnki.jccs.yg21.1707>

875 Wu, J., Wang, J., Liu, J., Yang, Y., Cheng, J., Wang, Z., Zhou, J., Cen, K., 2017.
876 Moisture removal mechanism of low-rank coal by hydrothermal dewatering:
877 Physicochemical property analysis and DFT calculation. *Fuel* 187, 242–249.
878 <https://doi.org/10.1016/j.fuel.2016.09.071>

879 Xu, C., Wang, D., Wang, H., Xin, H., Ma, L., Zhu, X., Zhang, Y., Wang, Q., 2017.
880 Effects of chemical properties of coal dust on its wettability. *Powder Technology*
881 318, 33–39. <https://doi.org/10.1016/j.powtec.2017.05.028>

882 Xu, H., Zhu, Y., Liu, H., Ding, H., Fang, H., Zhang, K., Jia, J., 2023. Wettability
883 alteration and dynamic wetting behavior of coal during geologic CO₂
884 sequestration using LF-NMR technology. *Fuel* 354, 129355.
885 <https://doi.org/10.1016/j.fuel.2023.129355>

886 Yan, J., Lei, Z., Li, Z., Wang, Z., Ren, S., Kang, S., Wang, X., Shui, H., 2020.
887 Molecular structure characterization of low-medium rank coals via XRD, solid
888 state ¹³C NMR and FTIR spectroscopy. *Fuel* 268, 117038.
889 <https://doi.org/10.1016/j.fuel.2020.117038>

890 Yan, J.-C., Bai, Z.-Q., Bai, J., Li, W., 2015. Chemical structure and reactivity
891 alterations of brown coals during thermal treatment with aromatic solvents. *Fuel
892 Processing Technology* 137, 117–123.
893 <https://doi.org/10.1016/j.fuproc.2015.04.009>

894 Yu, T., Li, Q., Li, X., Hu, H., Tan, Y., Xu, L., 2022. Synergistic effects of CO₂ density
895 and salinity on the wetting behavior of formation water on sandstone surfaces:
896 Molecular dynamics simulation. *Journal of Natural Gas Science and Engineering*
897 105, 104714. <https://doi.org/10.1016/j.jngse.2022.104714>

898 Zhang, R., Liu, S., Zheng, S., 2021. Characterization of nano-to-micron sized
899 respirable coal dust: Particle surface alteration and the health impact. *Journal of
900 Hazardous Materials* 413, 125447. <https://doi.org/10/gpmj7s>

901 Zhang, Y., Zheng, Y., Jiang, B., Yu, G., Ren, B., Yu, C., Wang, S., 2023. Experimental
902 study on the influence of acid fracturing fluid on coal wettability. *Fuel* 343,
903 127965. <https://doi.org/10.1016/j.fuel.2023.127965>

- 904 Zhao, D., Liu, X., Shen, Z., 2023. Effect of oxygen-containing functional groups on
905 the wettability of coal through DFT and MD simulation. *Arabian Journal of*
906 *Chemistry* 16, 104606. <https://doi.org/10.1016/j.arabjc.2023.104606>
- 907 Zheng, S., Yao, Y., Elsworth, D., Liu, D., Cai, Y., 2020. Dynamic fluid interactions
908 during CO₂-ECBM and CO₂ sequestration in coal seams. Part 2: CO₂-H₂O
909 wettability. *Fuel* 279, 118560. <https://doi.org/10.1016/j.fuel.2020.118560>
- 910 Zhou, J., Zhang, J., Yang, J., Jin, Z., Luo, K.H., 2022. Mechanisms for kerogen
911 wettability transition from water-wet to CO₂-wet: Implications for CO₂
912 sequestration. *Chem. Eng. J.* 428, 132020.
913 <https://doi.org/10.1016/j.cej.2021.132020>
- 914 Zhu, C., Wan, J., Tokunaga, T.K., Liu, N., Lin, B., Wu, H., 2019. Impact of CO₂
915 injection on wettability of coal at elevated pressure and temperature. *International*
916 *Journal of Greenhouse Gas Control* 91, 102840.
917 <https://doi.org/10.1016/j.ijggc.2019.102840>

918 Appendix A. Supplementary material

919

920 **Table A. 1** Mineral compositions of raw coal

Category	Common Minerals	Chemical formula
Silicate mineral (clay)	Kaolinite	$Al_4(Si_4O_{10})(OH)_8$
	Illite (hydromica)	$K_{1-1.5}Al_4(Si_{7-6.5}Al_{1-1.5}O_{20})(OH)_4$
	Chlorite	$(Mg,Fe,Al)_{12}[(Si,Al)_8O_{20}](OH)_{16}$
	Montmorillonite	$(Na,Ca)_{0.33}(Al,Mg)_2(Si_4O_{10})(OH)_2 \cdot nH_2O$
	Muscovite	$KAl_2(AlSi_3O_{10})(OH)_2$
Carbonate mineral	Calcite	$CaCO_3$
	Siderite	$FeCO_3$
	Dolomite	$CaMg(CO_3)_2$
Oxide mineral	Quartz (chalcedony)	SiO_2
	Hematite	Fe_2O_3
Sulfide mineral	Pyrite, marcasite	FeS_2

921

922 **Table A.2** Fitting peak information in XRD for calculating semi-quantitative
923 structural parameters

Peak type	Group	FWHM			2 (weighted average center)		
		γ -band	002-band	100-band	γ -band	002--band	100-band
Lorentz	Raw coal	7.06641	3.38373	6.7259	21.0724 6	25.6866	40.0116 9
Lorentz	scN ₂	5.92757	3.86474	7.86542	20.8189 5	25.7018	39.4358 3
Lorentz	scCO ₂	10.7562 8	3.08301	4.65443	21.5864 9	26.3988 1	44.1116 7

924

925 **Table A.3** Dynamic contact angle under gaseous N₂ ($P=20\text{bar}$, $T=25^\circ\text{C}$)

Time (hours)	Left-Adv.	Right-Adv.	θ_{adv}	Left-Rec.	Right-Rec.	θ_{rec}
0	28	28	28	24	23	23.5
24	33	31	32	23	22	22.5
48	29	30	29.5	25	19	22
72	31	27	29	26	19	22.5

96	30	29	29.5	23	22	22.5
----	----	----	------	----	----	------

926

927 **Table A.4** Dynamic contact angle under scN₂ ($P=120\text{bar}$, $T=45^\circ\text{C}$)

Time (hours)	Left-Adv.	Right-Adv.	θ_{adv}	Left-Rec.	Right-Rec.	θ_{rec}
0	29	28	28.5	21	21	21
24	29	28	28.5	22	21	21.5
48	26	23	24.5	20	17	18.5
72	28	25	26.5	22	20	21
96	27	26	26.5	21	21	21

928

929 **Table A.5** Time-dependent static CAs under N₂.

Time hours	Average static contact angle ($^\circ$)	
	gaseous N ₂	scN ₂
0	24	23
24	25	22
48	24	23
72	23	24
96	23	23

930

931 **Table A.6** Dynamic contact angle under gaseous CO₂ ($P=20\text{bar}$, $T=25^\circ\text{C}$)

Time (hours)	Left-Adv.	Right-Adv.	θ_{adv}	Left-Rec.	Right-Rec.	θ_{rec}
0	40.3	51.0	45.7	19.9	18.0	19.0
24	32.4	35.8	34.1	23.2	19.0	21.1
48	36.8	42.0	39.4	24.2	24.6	24.4
72	31.4	38.6	35.0	24.0	20.6	22.3
96	37.3	38.5	37.9	21.8	19.4	20.6

932

933 **Table A.7** Dynamic contact angle under scCO₂ ($P=120\text{bar}$, $T=45^\circ\text{C}$)

Time (hours)	Left-Adv.	Right-Adv.	θ_{adv}	Left-Rec.	Right-Rec.	θ_{rec}
0	93.4	89.6	91.5	36.4	33.2	34.8
24	91.0	85.8	88.4	33.4	30.8	32.1
48	95.0	89.6	92.3	46.0	42.0	44.0
72	94.0	92.5	93.3	42.5	45.7	44.1
96	96.0	93.0	94.5	52.2	47.0	49.6

934

935 **Table A.8** Time-dependent static CAs under CO₂.

Time(hours)	Static contact angle	
	gaseous CO ₂	scCO ₂
0	22.5	35.0
24	22.0	44.2

48	25.8	52.4
72	24.4	53.4
96	23.9	55.7

936